

# How to Manufacture Photonic Metamaterials

Apurba Paul and Gregory Timp\*

Metamaterials, which started off focused on optical and electromagnetic applications such as invisibility and “hyperlenses” with resolution beyond the diffraction limit, has now broadened in scope to include pretty much everything from wireless communications (antennas), lasers, computing, solar power, sports equipment, medicine; acoustics, structural mechanics and even air conditioning. Yet, the promises derived from these applications have not been exploited in earnest and the market for them has not grown much so far, likely because a facile and economical method for fabricating them without defect has not emerged. This review scrutinizes the methods used to manufacture metamaterials with the aim to remedy this shortcoming.

also proposed that a periodic array of splitting resonators (SRR) could show negative  $\mu$  in a specific frequency band.<sup>[22]</sup> What is new is that metamaterials, which started off focused on optical and EM applications like invisibility (stealth) and “hyperlenses” with resolution beyond the diffraction limit, now extend into pretty much everything from wireless communications (antennas), lasers, computing, solar power, sports equipment, medicine (health-care), acoustics (ultrasonics), structural mechanics and even air conditioning. Yet, despite the “zoo” of applications,

there is only a scant market for them, which was expected to reach \$0.22 billion (US dollars) in 2024 mostly driven by the demand for EM and photonic metamaterials (PMs), in particular.<sup>[23]</sup>

The lackluster market for PMs may be due to the difficulty of making them. At its core, PMs rely on sub-wavelength inclusions—which are on a nanometer-scale for visible light that resonantly couple to the electric and magnetic fields of light to produce extraordinary optical properties such as a negative index of refraction. Due to their complexity, there are at least two stumbling blocks that stymie the manufacture of PMs: 1. making them with enough precision to avoid losses due to random scattering (i.e. precise registration over a wide field); and 2. developing a scalable economical manufacturing process that can accommodate the peculiar constituents and is still robust enough to put them to work in diverse applications. So, the promise of metamaterials won't be fully realized until nanometer-scale structures can be assembled together, inexpensively, into a working system without defect. To that end, right now, there are mainly two strategies that have been used to create metamaterials; both elicit aspects of the promise, but they remain problematic nevertheless. The first is the “top-down” method like that used to fabricate integrated electronic circuits (ICs), for example. The second is the “bottom-up” approach like that used to synthesize antibiotics, for example. The successful implementation of these strategies for producing ICs and antibiotics are glaring examples and make conspicuous targets to aim at in the manufacture of a metamaterial. To illustrate the promise and the problems and, at the same time, map out a path forward for the manufacture of PMs, let's first unpack these two examples to see what they're doing right.

“Top-down”: Currently, at the “3 nm” node, Taiwan Semiconductor Manufacturing Corporation (TSMC) can produce a monolithic IC consisting of 300 million transistors per square millimeter (Figure 2), while International Business Machines Corporation (IBM) has apparently bettered that by producing a chip the size of a finger nail (1 cm<sup>2</sup>) with nearly 50 billion transistors at the “2 nm” node.<sup>[24]</sup> These innovations will likely find their way

## 1. Introduction

Metamaterials are unnatural. Their architecture comprises artificial “atoms” and “molecules” decorating a (what may be on purpose and otherwise unintentionally defective) lattice with a shape and size tailored by a variety of means to elicit a refractive index near-zero or even negative (Figure 1).<sup>[1–16]</sup> They can be 3D constructions or so-called meta-surfaces constrained to a thin, quasi-two-dimensional (2D) layer. The idea is not new. Maxwell discussed the possibility of laminates like this in 1873<sup>[17]</sup> and in 1898, Bose experimentally showed that twisted structures (chiral materials) can produce artificial linear and circular birefringence.<sup>[18]</sup> In 1968, Veselago described the reflection and refraction of electromagnetic (EM) waves in materials simultaneously having a negative dielectric constant ( $\epsilon$ ) and magnetic permeability ( $\mu$ ).<sup>[19]</sup> Later in 1998, Pendry *et al.* demonstrated that a periodic array of thin metal wires can produce an electromagnetic response that corresponds to negative  $\epsilon$  by reducing the plasma frequency.<sup>[20,21]</sup> A bit later than that, in 1999, they

A. Paul  
Department of Electrical Engineering  
University of Notre Dame  
Notre Dame, IN 46556, USA

G. Timp  
Department of Electrical Engineering and Biological Science  
University of Notre Dame  
Notre Dame, IN 46556, USA  
E-mail: [gtimp@nd.edu](mailto:gtimp@nd.edu)

The ORCID identification number(s) for the author(s) of this article can be found under <https://doi.org/10.1002/admt.202500313>

© 2025 The Author(s). Advanced Materials Technologies published by Wiley-VCH GmbH. This is an open access article under the terms of the [Creative Commons Attribution-NonCommercial](#) License, which permits use, distribution and reproduction in any medium, provided the original work is properly cited and is not used for commercial purposes.

DOI: 10.1002/admt.202500313

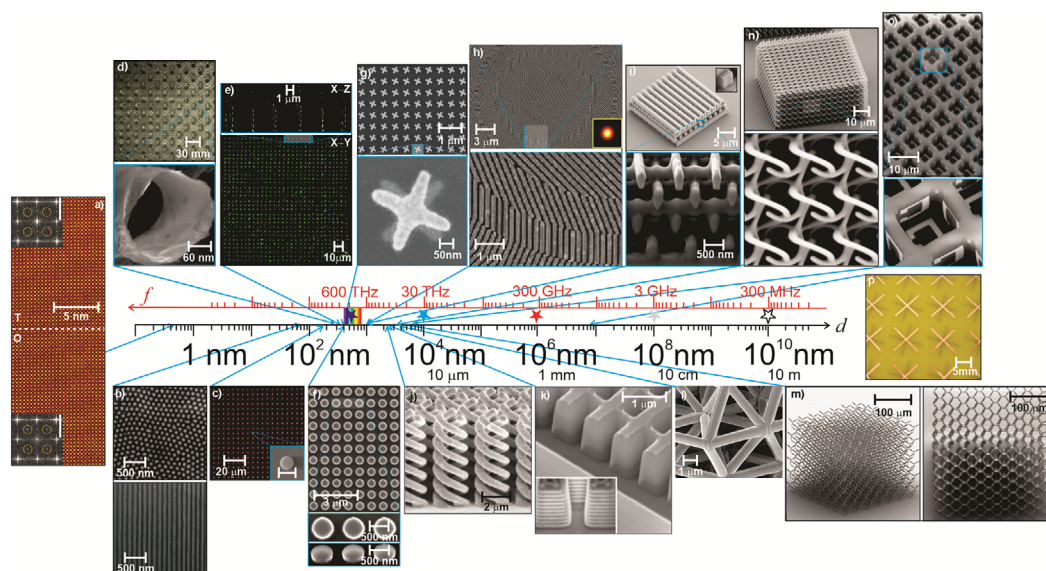


**Figure 1.** Metamaterials by scale and frequency. The minimum (maximum) feature size, which is labeled “*d*” (frequency labeled “*f*”) for each metamaterial is indicated by the blue arrows on the two scales. For reference, the visible band is illustrated by the rainbow embedded in the scale. The stars delineate five especially useful bands in the spectrum: blue—visible light; cyan—resonances such as plasmonic effects and rotational states of molecules; red—millimeter wave communication, radio astronomy; light blue—5G networks; and white—NMR spectroscopy, television broadcasts amateur radio, ultrasound. a) A cross-sectional, high-resolution scanning transmission electron micrograph (HR-STEM) (false color) of the interface between the tetragonal (T) and orthorhombic (O) phases in a 30 nm thick *La*-doped *SrSnO<sub>3</sub>* with an undoped 108 nm thick *SrSnO<sub>3</sub>* buffer layer on a *GdScO<sub>3</sub>* (110) substrate. These periodic nanostructures were self-assembled using a T-to-O martensitic phase transformation. The insets show selected area Fourier transforms with a scale of 3 nm<sup>-1</sup>. Adapted from ref. [33] b) (top) Scanning electron micrograph (SEM) of nanowires embedded in an alumina matrix are shown. b. (bottom) A side view of the same nanowires. The wires have a 60-nm diameter and 110-nm center-to-center distance. Adapted from ref. [12]. c) Array of several hundred (~160 nm diameter) amorphous *Si* nanoparticles (NPs) fabricated by laser ablation and visualized with dark-field microscopy. The insert shows an SEM of a single *Si* NP in this array. Adapted from ref. [1]. d) (top) An optical micrograph of a *Ni-P* alloy hierarchical metamaterial spanning seven orders of magnitude in length, fabricated with additive manufacturing employing large-area projection micro-stereo-lithography that uses a spatial light modulator in conjunction with an optical scanning system. d) (bottom) The structural hierarchy of the multiscale metamaterial extends from 5 cm to tens of nanometers in wall thickness of the *Ni* nanotubes. Adapted from ref. [14] e) (bottom) A fluorescence confocal image of a three-dimensional metamaterial assembled from 350 nm diameter polystyrene NPs using the light gradients in a time-shared Bessel-beam optical standing wave. A 10 × 10 super-lattice was formed out of voxels consisting of 3 × 3 × (*X* > 10) sub-lattices with the “step-and-repeat” method. e) (top) A reconstruction formed from the confocal image of the same metamaterial, but de-convolved to reveal the lattice structure along the optical (*z*) axis. The  $\lambda/2n = 320$  nm spacing due to the standing wave along the *z*-axis was easily resolved to reveal that the NPs must abut each other. Adapted from ref. [10] f) (top) SEM of typical *Si* nanodisks fabricated on an SOI wafer using electron beam lithography in combination with reactive ion etching are shown before embedding them into the low-index medium. f) (middle, bottom) SEMs showing magnified normal and oblique-incidence views, respectively of the same array. The *Si* disks range from 400–600 nm in diameter and are 220 nm thick. Adapted from ref. [11] g) (top) An SEM normal, large-area view of a chiral metamaterial structure composed of right-handed twisted gold crosses fabricated using electron-beam lithography in combination with a spin-on dielectric, planarization and reactive-ion etching. g) (bottom) Magnified oblique-view SEM of the structure highlighted in blue in g, top. The arms of the gold double crosses have a thickness of 25 nm, a full width of 56 nm and a length of 315 nm. The double crosses are arranged on a simple square lattice with a lattice constant of 500 nm. Adapted from ref. [13] h) (top). An SEM image is shown of a dielectric gradient meta-surface optical element with a focal length of 100 μm at  $\lambda = 550$  nm. h) (top, right lower inset) The 2D intensity profile in the focal plane is shown. h) (bottom) A magnified view of the area highlighted in blue in h, top. Adapted from ref. [4] i) (top) An SEM of an *As<sub>2</sub>S<sub>3</sub>* woodpile with rod distance 2 μm fabricated using direct laser writing is shown, but now viewed along the (001)-direction to reveal the hexagonal sub-structure of the diamond crystal. The volume filling fraction is estimated to be 1.5% and a total metamaterial weight of 270 ng. Adapted from ref. [2] n) (top) Oblique view on a right/left-handed polymer structure made by direct laser writing is shown. The cubic lattice constant of the structure is about 4 μm. n) (bottom) The diameter of the spiral is about 3.6 μm. Adapted from ref. [5] o) (top) Low resolution SEM of a metamaterial consisting of split-ring-resonators (SRR) produced using self-aligned, membrane projection (electron-beam) lithography. o) (bottom) High resolution SEM of the composite unit cell with 5 split-ring-resonators. Each cell is 3.0 μm on a side and each trace has a width of 0.7 μm with a gap of 0.6 μm. The cubic array has a lattice constant of 6 μm. Adapted from ref. [9] p) Photograph of one side of a fabricated microwave-scale bi-layer, cross-wire, chiral metamaterial; the length (width) of the wires comprising the crosses are 14 (0.8) mm, presumably printed onto a photosensitive film on copper using a high-precision plotter. subsequently the copper foil was etched. The thickness of the copper is 36 μm. Adapted from ref. [7]

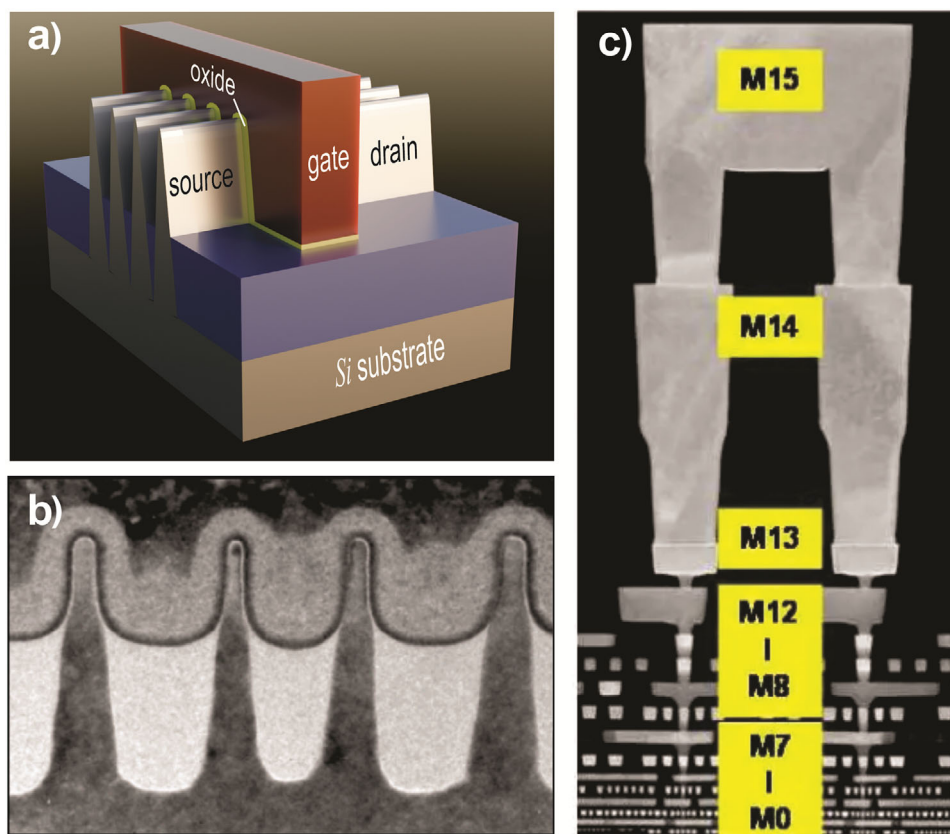


**Figure 2.** The front- and back-end characteristics of the “3 nm” node in semiconductor manufacturing according to IMEC and TSMC. a) A schematic representation of a FinFET showing that it has thin vertical “fins” instead of being completely planar. b) TEM cross-section of an IMEC FinFET. The fin-width is 4.5 nm and the fin-height is about 26 nm. c) A cross-section through the metal backend of the TSMC N3 process is extremely dense. The metal0 pitch (M0) is 23 nm. Adapted from refs. [27a,b].

into the iPhone 17 series next year, and iPhone 18 Pro models in 2026.<sup>[25]</sup> Despite the apparent success, problems still plague this “top-down” technology. TSMC’s “3 nm” process is based on a FinFET process flow.<sup>[26]</sup> A FinFET is a type of field-effect transistor (FET) that has a thin vertical fin instead of being completely planar (Figure 2a,b). The gate, which is separated from the channel formed between the source and the drain by an effectively thin dielectric layer, “wraps” around the channel on three sides in a FinFET to afford more control over the current between source and drain in the ON-state, and reduce the leakage in the OFF-state relative to a planar FET. However, a “3 nm” or “2 nm” transistor doesn’t actually measure 3 nanometers in any dimension; it’s a bit of a misnomer. Instead the term just refers to the overall manufacturing process node, which is an advertising ploy illustrating higher performance per watt efficiency or higher transistor density or increased drive current. While the smallest feature size within the transistor like the gate dielectric thickness may be around 3–6 nm, the entire transistor itself is significantly larger with features like the gate pitch (the distance between the gates of two transistors in logic) and tightest metal pitch that are often much larger ( $\approx 48$  and 24 nm respectively, according to current industry standards).<sup>[27]</sup>

To avoid contamination, an IC incorporates only a restricted number of materials including Si, SiGe, SiN<sub>x</sub>, SiO<sub>2</sub>, exotic gate oxides such as HfO<sub>2</sub>, and Hf, Zr, TiN, Al, Cu to name a few. These

are meticulously designed, assembled and stacked into a 3D circuit using a combination of sophisticated computer-aided design (CAD) tools for the layout of the circuits and to model the process flow, utilizing a process that involves the exquisitely precise lithography, deposition and etch to carve the circuit elements and the interconnections between them to produce finally an IC from a single crystal wafer of silicon.

Moore’s law, the empirical projection that the number of transistors in an IC doubles about every two years at a minimal increase in cost, is failing. It depends on the cheap miniaturization of the transistor in an IC, but the transistor is butting up against physical (a channel only a few atoms long) and technological (13.5 nm Extreme Ultra-Violet—EUV lithography) limitations. Packing more and more transistors into a plane has just become impracticable. So, to rescue Moore’s law, multiple layers of transistors are now vertically “stacked” together either through monolithic integration (i.e. through monolithic 3D IC manufacturing—M3D) or by bonding multiple layers fabricated separately.<sup>[28,29]</sup> The vertical integration between the layers allows for shorter interconnections, which in turn results in faster signal transmission, reduced signal delay and higher operating speed with greater efficiency.<sup>[29–32]</sup> Another major advantage of 3D stacking is the reduction in power consumption. As the interconnection becomes shorter, the power loss shrinks compared to planar electronics.

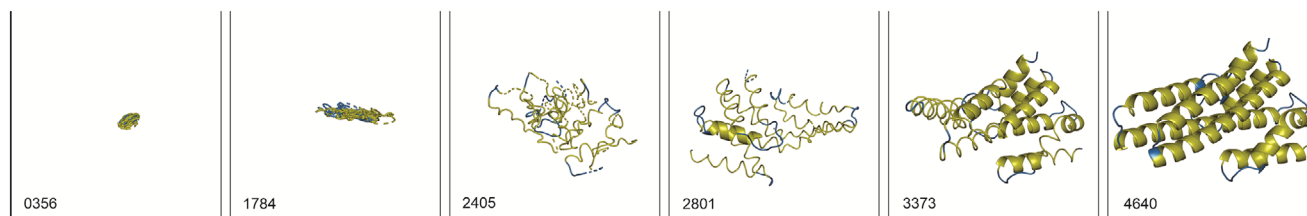


**Figure 3.** Folding animation for PDB protein 7DMF, chain A) These predictions are from successive early checkpoints of an OpenFold model. The training step is shown in the bottom left corner. OpenFold predicts protein structure by starting with the primary structure—the disordered amino acid sequence (left)—and then homes in on the secondary structural elements and eventually reaches 3D form for the protein (right). The fold starts from the amino acid sequence for 7DMF-chain A, which is: DCQQELSLVQTVTRGSRAFLSREEAQHFVKECGLLNCEAVLELLICHLRL GMEIMKLGRLREAVRANDVDAMLKIAKEIKVIGETGLDEVYRQLLKAKEFLERRAENFSHEEVAFAQQIILQIKQVECVQMRALGAVASLGCTDLLPQEIHILLTRPRLQELSAAGSPGVTNKATKILRHFEASC. Adapted from refs. [38,39].

What's especially problematic though about the “top-down” approach to the “3 nm” node is that it is time-consuming to manufacture and very expensive. An advanced process flow consists of thousands of steps involving more than 100 mask layers (as many as 19–25 EUV lithography layers) with up to 19 metal levels and it can take >3 months to push a wafer from design through production. On top of that, the process is expensive—it costs  $\approx$  \$40 per  $\text{cm}^2$  of silicon to produce a chip at the “3 nm” node (or \$18,000 to \$20,000 per 300 mm or 12” wafer).<sup>[33]</sup> Moreover, the cost of a semiconductor fabrication facility to process the wafer in an ISO Class 1 cleanroom environment (i.e. <2 particles greater than 0.3  $\mu\text{m}$  and no particles greater than 1.0  $\mu\text{m}$  per cubic meter like the Samsung's fab in Taylor, Texas) is projected to be north of \$22 billion in 2025. The fab equipment by itself is estimated to cost more than \$15–20 billion for the “3 nm” node.<sup>[34]</sup> What's especially onerous is that, after all that investment of time and money, the chip may be defective. Although it is generally a closely guarded trade secret, the yield of the one gigabyte double data rate 3 (1 GB DDR3) memory module that used to store data for quick access by the central processing unit (CPU) off-the-line goes from 0% to  $\approx$  70% only with repair and because of redundancy.<sup>[35]</sup> Samsung and TSMC yields could sink as low as 20%.<sup>[36]</sup> But so far, the market for ICs still drives these expenditures; the world market for ICs alone is projected to top \$602 billion in 2025 and grow from there.<sup>[37]</sup>

**“Bottom-up”:** On the other hand, to create antibiotics, pharmaceutical companies use a “bottom-up” approach that usually involves combinatorial chemistry to create libraries from a range of peptides, non-peptide oligomers, peptidomimetics and small-molecules that are meant to target a specific infection. Once they're synthesized, the peptides in the library can be screened concurrently to “kill” the biological target. However, the vast majority of antibiotics discovered so far have insufficient biological activity, toxicity issues, or unfavorable pharmacokinetics to be developed into a drug as a curative for humans. It seems likely that's about to change, however.

The native, 3D-shape of a protein dictates its chemistry and efficacy. The primary structure of a protein is constituted by amino acid residues linked in a chain by peptide bonds—the information content resides there. The information embedded in the primary structure affects if and how a protein folds from an unstable random coil into a more ordered, specific 3D structure (Figure 3). Folding relies on weak, non-covalent bonds such as

hydrogen bonds, ionic bonds, van der Waals forces and/or hydrophobic and hydrophilic interactions to autonomously force the aggregation of specific amino acid residues into a stable native structure. And it does so repeatedly with sub-nanometer precision! Thus, (aside from chaperones that are sometimes used to guide it), the 3D structure of a protein is usually dictated by equilibrium thermodynamics without appealing to the specific pathway describing how it got there.<sup>[41]</sup> However, when the specific 3D structure of a protein is demolished—the function is lost. So, the stability of the native structure is vitally important. How a protein folds or mis-folds is then the key to an efficacious therapeutic—protein folding, degradation, aggregation, solubility, crystallization and fibrillization all have to be scrupulously managed.

Now it seems that it is possible to predict how a protein will fold using computer simulations or artificial intelligence (AI) like AlphaFold2/Google Deep Mind, OpenFold/Meta AI, SyntheMol.<sup>[38–41]</sup> For example, AlphaFold2 steers clear of physics-based models that have frustrated molecular dynamics simulations of folding so far, in favor of deep learning.<sup>[41]</sup> The code scans documented, reference sequences looking to learn about the similarities to the query and detect changes in sequences that may have co-evolved and so, are likely to be close to one another in space when a protein folds. Along those same lines, OpenFold is even faster at it than AlphaFold2, but just as accurate and it can be retrained easily (Figure 3).<sup>[38,39,41]</sup> Using OpenFold, in conjunction with a language model like ChatGPT, Meta AI was able to release the structures of more than 600 million little-known proteins recently, which may eventually obviate the need for combinatorial chemistry and facilitate screening in drug discovery altogether. The proof is in the pudding: *SyntheMol*, a generative AI model, has been used to design easy-to-synthesize antibiotic compounds using known molecular building blocks and synthesis reactions.<sup>[40]</sup>

At its root, protein folding is just another example of “self-assembly.” Generally, “self-assembly” uses weak, typically non-covalent bonds to autonomously force the aggregation of molecules or components like micro- or nanoparticles (NPs) into stable 3D structures.<sup>[42–47]</sup> But, “self-assembly” is limited to the formation of structures that represent kinetically trapped states or a thermodynamically minimum energy and, because of the weak binding energy, “self-assembly” tends to produce systems that are defective. For example, there is an untoward propensity for hydrophobic amino acid side chains in a protein to aggregate

beyond the design, which can lead to the formation of amyloid deposits that have been implicated in human pathologies such as Alzheimer's disease.<sup>[48,49]</sup> It's estimated that up to one-third of newly synthesized proteins may be degraded due to folding issues.<sup>[50]</sup> The price is astronomical and the cost is reflected in drug discovery for antibiotics. For example, it can take 10–15 years to bring a new antibiotic to market, but initially identifying the antibiotic and optimizing the structure can be costly even before a clinical trial begins. The break-even cost to the pharmaceutical industry to produce a single drug (which is inextricably tied to clinical trials of the efficacy of a protein, not just protein synthesis) tops \$1.7 billion currently.<sup>[51]</sup> However, the global market for antibiotics is still compelling; it is projected to reach \$56.8 billion in 2025.<sup>[52]</sup>

So, we've been schooled. Notice the common lessons apparent from these two success stories are: i.e. 1. implementation through the use of computer-aided design (CAD); 2. there is a restricted number of constituents; 3. volume manufacture sets the rules; and finally, 4. unintentional defects are pervasive and costly. Generally, regardless of the method, the costs increase with the complexity of the process.

Right now, the global market for PMs is miniscule in comparison to ICs or antibiotics and PMs will likely suffer similar challenges or worse. Due to coherence, unintentional defects, such as variations in the unit cell geometry or localized (topological) distortion are especially detrimental. Such defects can compromise functionality by shifting or eliminating bandgaps, affecting scattering, transmission and reflection of an electromagnetic wave. For example, according to Li and Zhang,<sup>[53]</sup> in the presence of disorder such as variations in the radii of air spheres and their positions, the bandgap reduces significantly, and closes at a fluctuation magnitude as small as under 2% of the lattice constant. Restrictions like this impose a severe requirement on the uniformity of the PM lattice.<sup>[54]</sup> Likewise, and just as relevant, in metamaterial mechanics, defects can lead to changes in elastic modulus and compressive strength that affects the long-range order.<sup>[55]</sup>

So, how do we “light up” metamaterials and bring them successfully to market? To gain some perspective on the prospects and fairly assess the implications, let's review and compare strategies for the manufacture of PMs starting with the “top-down” and “bottom-up” methods that have been employed so far. There is no pretense to be comprehensive here. There is already a glut of very informative reviews that tackle metamaterials,<sup>[56–69]</sup> the fabrication of them,<sup>[70–76]</sup> along with their applications (like imaging).<sup>[57,63–65,69,74–78]</sup> So, in a way less than exhaustive in scope, this review focuses narrowly on PMs and analyzes tersely certain aspects of well-worn “top-down” and “bottom-up” methodologies looking at the strengths and weakness peculiar to their fabrication that go beyond those already outlined by the two prime examples, i.e. ICs and antibiotics. The methods are assessed with two particular applications in mind: a lens and an antenna.

**First**, “top-down, layer-by-layer” fabrication of PMs using (2D) lithography in combination with deposition and etch or “lift-off” are scrutinized to produce metamaterials like those illustrated in Figures 1c,f,g. **Next**, the methods used for “top-down, 3D printing or additive manufacturing (AM)” of PMs like those illustrated by Figures 1h,i,j,l,m are examined to discover their advan-

tages and expose their limitations. **Then**, schemes for “bottom-up” self-assembly to form metamaterials like those illustrated in Figure 1a are explored<sup>[79,80]</sup> that rely on block co-polymers,<sup>[81]</sup> dendritic molecules,<sup>[82]</sup> DNA origami,<sup>[83]</sup> or colloidal clusters for creating PMs and intense lasers.<sup>[84–87]</sup> **And finally**, “for something completely different”—a method for the manufacture of PMs is introduced (Figure 4) that works just like modular construction—borrowing from both the “bottom-up” practices for synthesizing nanoparticles (NPs) and from “top-down” methods that uses light gradients in conjunction with a “step-and-repeat” process—to assemble the NPs into “voxels” that form 3D-PMs like that shown in Figure 1e.<sup>[10]</sup> PMs have been fabricated using “top-down” or “bottom-up” methods before, but not this way.

Using light gradients to assemble NPs is not science fiction anymore. In a pilot study this alternative was tested and it seems viable too.<sup>[10]</sup> **First**, using low temperature, chemical solution methods that offer economical and scalable synthesis, monodispersed, nanoparticles (NPs) with built-in functionality are formed with a coefficient of variation,  $CV < 1\%$ . **And then** the NPs are conveyed, using multiple laminar flows in a multi-port microfluidic device within the field of view and shepherded into an array of time-shared optical traps formed from a standing wave, Bessel beam over a “hot” mirror (i.e. a mirror that reflects infrared light while allowing visible light to pass). Thus, the gradient force in the optical traps is put to work assembling a (homogeneous or heterogeneous) collection of thousands of NPs into “voxels” on a hydrogel scaffold (at least temporarily).

This alternative strategy for manufacturing is especially timely. It straddles two contemporaneous revolutions that are churning right now: one in optical manipulation,<sup>[88]</sup> and another in photonics.<sup>[89]</sup> The feasibility of using optical tweezers to manipulate particles had already been demonstrated in pioneering work on atoms, molecules, microspheres, and living cells and organelles.<sup>[90–102]</sup> The basic forces derived from a focused laser beam acting on a small particle are well known<sup>[103–117]</sup> and theoretically they can be comparable to or exceed the strength of a hydrogen bond, depending on the topography of the optical field and on the properties of the particle and surrounding medium. Light gradients have been used to manipulate metallic<sup>[118]</sup> or dielectric,<sup>[102–105]</sup> low index, high index<sup>[119]</sup> or highly reflecting, nano- or micro-particles, in liquid or in air.<sup>[111,113]</sup> The prospects for using the same physics to organize more complex systems with nanometer precision is just now being explored. For example, an optical standing wave has been utilized to position atoms on a substrate with nanometer-scale resolution and sub-nanometer registration derived from an atomic clock.<sup>[90–94]</sup> The same type of optical fields have been used to create regular arrays of microspheres.<sup>[44,97–99,120–127]</sup> Now, with the development of multi-functional traps<sup>[120]</sup> and optical trap arrays,<sup>[97–99]</sup> tweezers can be used to rapidly<sup>[128]</sup> interrogate many points in space and time, and even induce chemical as well as physical transformations.

## 2. Metamaterials: Why They are Fabricated

PMs have been used to steer light,<sup>[129]</sup> polarize wave fronts<sup>[130,131]</sup> and generally manipulate the phase of electromagnetic radiation.<sup>[132,133]</sup> At first, metallic nanostructures fabricated

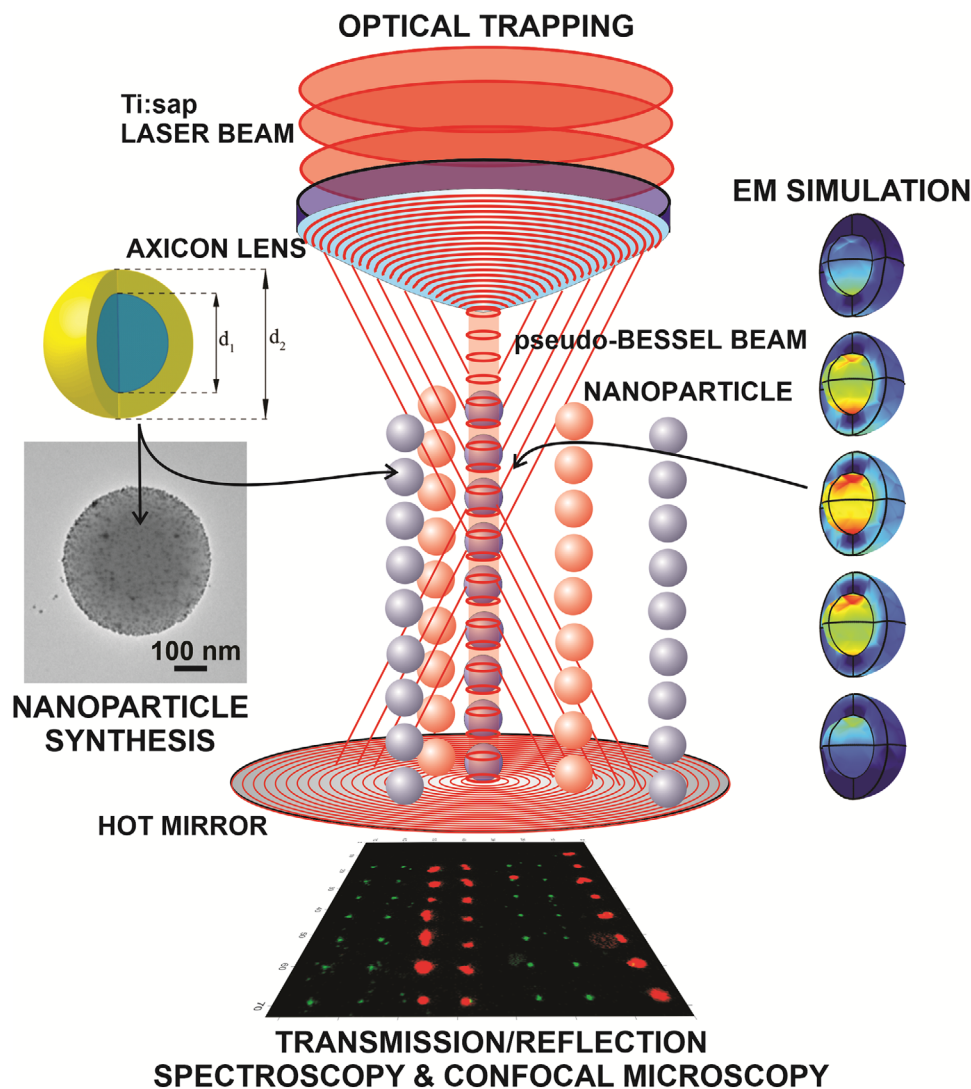


**Figure 4.** Modular nanofabrication of metamaterials. There are three aspects of this tool represented in this schematic: nanoparticle synthesis; optical trapping and EM simulation. Optical trapping is at the core of the effort. The central feature in the figure is a schematic representation of time-shared optical trap used to assemble a metamaterial. Top center: A pseudo-Bessel beam standing wave optical trap (red) is formed by focusing a Ti:sap laser through an axicon lens onto a “hot” mirror (represented red). The traps, which are rastered from site-to-site, are used to assemble on a heterogeneous metamaterial on a (photopolymerized) hydrogel scaffold, represented by lines of (different colored) nanoparticles in the figure. The metamaterial is modular, consisting of different types of nanoparticles (e.g. *Au*, *Si*, core-shell). Left: A TEM image of a core-shell nanoparticle with a 500 nm-diameter  $\text{SiO}_2$  core and a 5 nm *Au* shell is shown. Right: Electromagnetic simulations are used to both design scattering resonances into the nanoparticles and specify the layout to produce a PM. Bottom: Finally, following assembly, the metamaterial is vitrified with TEOS and characterized using angle-, wavelength-, and polarization-dependent transmission and reflection spectroscopy along with confocal microscopy.

with lithography, metal deposition and etching, were used to produce PMs, but the process flow was not really commercially viable—it was error-prone and costly.<sup>[14,134–139]</sup> Regardless, the optical losses were intolerable especially when multiple metal-based layers were stacked together. For example, according to Soukoulis and Wegener,<sup>[61]</sup> the best measured value for the  $1/e$  intensity decay length is around a quarter of a wavelength inside passive double-fish-net negative-index PMs. On the other hand, meta-surfaces made by patterning deep sub-wavelength thickness metals or high refractive index dielectrics can be implemented instead to side-step the hurdles associated with 3D nanofabrication while at the same time minimizing optical

losses by shortening the optical path length.<sup>[71,136,137]</sup> However, according to Shalaev,<sup>[139]</sup> stability remains a problem. Metals like *Au* and *Ag*, which have been used as plasmonic conductors, melt. In lieu of *Au* or *Ag*, *TiN*, *Zr*, and hafnium nitrides may offer alternatives because they melt at higher temperatures. In particular, *TiN* has optical properties like *Au* and is not only thermally stable at high temperature, but has the extra added bonus that it is compatible with semiconductor manufacturing. Alternatively, and even simpler, it has become apparent that PMs can be formed from dielectrics in which the displacement current replaces the Ohmic currents in the metal. For example, by leveraging Mie scattering resonances from dielectric NPs,

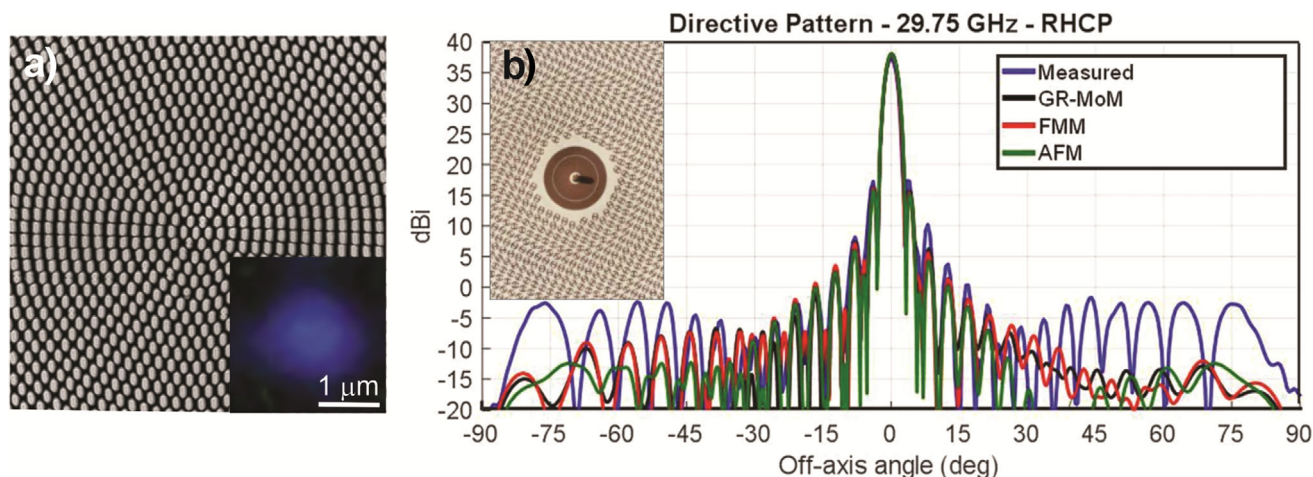


**Figure 5.** Meta-lens and meta-antenna. a) A scanning electron micrograph (SEM) of an on-axis focusing meta-lens. a. (inset) Measured intensity distribution at the corresponding focal plane. The meta-lens is designed with diameter of 100  $\mu\text{m}$  and focal length of 300  $\mu\text{m}$ . It works in a transmission window with extremely high operation efficiency of 91.6% in visible light. Adapted from ref. [143]. b) Co-polar 37 dB directive gain patterns by a meta-surface antenna operating at 29.75 GHz designed with product tapering spill-over efficiency of 85%. Curves show a comparison of measurements (blue line) with three types of numerical predictions: the Adiabatic Floquet mode (AFM) method; the Gaussian ring Method of Moments (GR-MoM); the full-wave fast multi-pole method (FMM) of analysis for the textured layout. (b, inset) The details of the feed illustrating the pixels used to implement the meta-surface antenna. The elements gradually change from cell-to-cell, but at the frequency of operation, they are small compared to the wavelength  $< \lambda/5$ . Adapted from ref. [160].

negative magnetic permeabilities and electric permittivities can be produced this way.<sup>[58–65,140]</sup>

Among a legion of applications, there are at least two categories: lenses and antenna design (Figure 5). The elements comprising the applications are usually small compared to the wavelength (in the range from  $\lambda/5$  to  $\lambda/10$ ) and change subtly from cell-to-cell. It is the phase relationship between the elements comprising a lens or antenna that's critical to the performance. Consider this “toy” model (Figure 6a) that captures aspects of both applications. In the far field, where the distance  $r$  from the array is much larger than the elements or the distance between them, if each of the elements comprising the (perfectly

uniform) 1D metamaterial is represented naively as a collection of simple Hertzian (infinitesimal) dipoles, then the electric field,  $E$ , due to a (1D)  $N$ -element array looks like:

$$|E(\theta)| = \underbrace{\left| \sqrt{\frac{\mu}{\epsilon}} \cdot \left( \frac{2\pi}{\lambda} \right) \cdot \frac{\Delta z \sin \theta}{4\pi r} e^{-i(2\pi/\lambda)r} \right|}_{\text{Hertzian}} \cdot \underbrace{\left| \frac{\sin(N[(2\pi/\lambda)d \cos \psi + \delta\alpha]/2)}{\sin[(2\pi/\lambda)d \cos \psi + \delta\alpha]/2} \right|}_{\text{array}} \quad (1)$$

where  $\theta$  represents the angle from the normal,  $\psi = \pi/2 - \theta$ , and  $\varphi$  is the azimuthal angle,  $d$  is the distance between elements,  $\lambda$  is the wavelength,  $\delta\alpha$  denotes the phase shift between individual elements in the array and  $\Delta z$  is a measure of the size

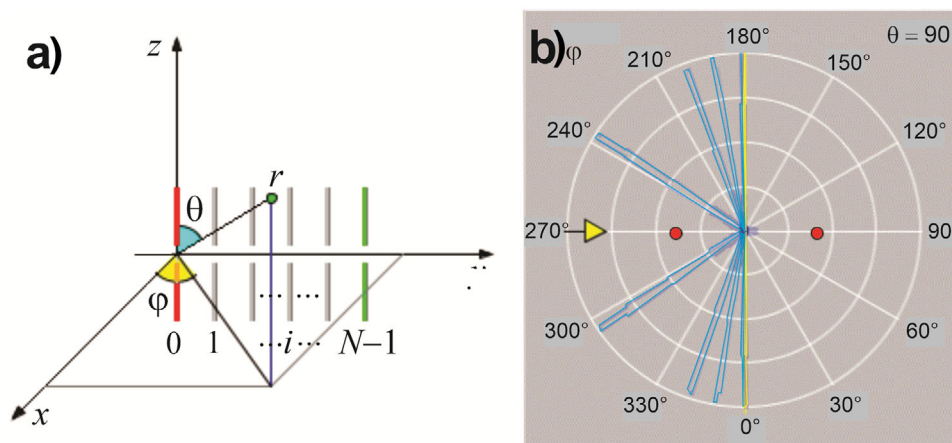


**Figure 6.** A “toy” model for a 1D-metamaterial. a) Schematic showing an array of (50) Hertzian dipoles. The dipoles in the array are assumed to have a uniform phase delay  $\delta\alpha$  that is independent of the spacing between dipoles  $d$ . b) The electric field distribution is shown for an array of  $N = 50$  dipoles for phase delays of  $\delta\alpha = 0^\circ, 30^\circ, 60^\circ$  and  $90^\circ$  to illustrate the sensitivity of the radiation pattern to the delay, which could result from a registration error between 1D arrays.

(strength) of the infinitesimal dipole. This equation illustrates some of the principles guiding the design of a phase array antenna and it shows the delicate relationship that exists between the wavelength, the distance between elements and their size. It shows that the array factor in the radiation pattern peaks in the azimuthal plane ( $\theta = 0$ ) when  $(2\pi/\lambda)d\cos\psi + \delta\alpha = 0$ ,  $2\pi, \dots$ , but nulls when  $N[(2\pi/\lambda)d\cos\psi + \delta\alpha] = 2m\pi$ , for integer  $m$  so long as  $m \neq 0, N, 2N, \dots$  (Figure 6b). With increasing  $N$ , the radiation pattern narrows to a pencil (with a spread of  $\approx 6^\circ$  for  $N = 50$ ) beyond  $N = 20$  and moves continuously with changes in  $\delta\alpha$  as it ranges from  $0^\circ$  to  $30^\circ$ ,  $60^\circ$  and  $90^\circ$  finally. This is important because  $\delta\alpha$  captures the incremental phase delay between one array and another in this “toy” model illustrating the sensitivity to registration  $\delta\alpha$ . Relationships like this are the key to the far-field performance.

Metamaterials are not natural. They exhibit a negative index of refraction, combining a negative dielectric constant ( $\epsilon$ ) with a negative magnetic permeability ( $\mu$ ) to produce double negative  $\epsilon$  and  $\mu$  over some frequency range. They’ve attracted special attention for a reason. The propagation of the electromagnetic wave through a negative index material (NIM) is reversed. Materials with a negative refractive index bend light at a negative angle to the surface normal causing the light from a point source to converge back to a point. Thus, a NIM focuses all the spatial frequencies from a 2D image to a plane creating what’s been called a perfect lens.<sup>[141,142]</sup> But this kind of lens is actually imperfect, since it does not have a proper focal length. Instead it works for only a specific range of object distances.<sup>[65,143,144]</sup> What’s more, evanescent waves that carry information at high spatial frequencies are amplified and propagate further in a NIM and, since the phase travels backward, a NIM can focus light below the diffraction limit.

Whereas a regular glass lens is usually curved and suffers diffraction, resolution below the diffraction limit becomes possible with a “hyperlens” or meta-lens even with a flat surface, at least in principle. “Hyperlenses” and meta-lenses (a meta-surface-based lens)<sup>[65,143,144]</sup> can be made from highly asymmetric metamaterial with opposite signs for the perpendicular and parallel permittivities,  $\epsilon_\perp$  and  $\epsilon_\parallel$  respectively.<sup>[142,145,146–153]</sup> Theoretically, such material allows for the propagation of evanescent waves, which carries sub-wavelength information,<sup>[152]</sup> and in a cylindrical geometry, sub-wavelength features have actually been magnified this way but so far, metamaterial lenses cannot focus a plane wave. According to Lu and Liu,<sup>[153]</sup> there are two essential requirements for creating a hyperlens or meta-lens out of metamaterial for (far-field) sub-diffraction imaging: 1. a material that supports wave propagation with high wave-vectors; and 2. a magnification mechanism that converts high wave-vector waves to low wave-vector waves so that super-resolution information can be sent to the far-field. Along with super-resolution information, a metamaterial lens also requires a phase compensation mechanism. This was first accomplished by combining a plasmonic metal-insulator-metal waveguide coupler with a metamaterial.<sup>[154]</sup> One example is a metamaterial immersion lens (MIL) that achieves focus by using a curved surface (convex for elliptic and concave for hyperbolic) along with the sub-diffraction limit focusing due to the metamaterial.<sup>[155]</sup> Another type is the gradient-index (GRIN) meta-lens, which has a flat geometry, but gradually varying refrac-

tive index in which the permittivity is designed to achieve both a focussed plane wave as well as the sub-diffraction limit resolution imaging.<sup>[156,140]</sup>

Metamaterials can radically affect antenna design too through miniaturization, gain enhancement and decoupling (Figure 6b).<sup>[157–175]</sup> Miniaturization of antennas translates to reducing the physical size of the antenna, without compromising the performance. Several approaches for miniaturization of an antenna have been tried, but just reducing the aperture size also degrades the efficiency and radiation characteristics. Metamaterials offer a solution. In one approach, Mahmoud<sup>[169]</sup> demonstrated that a circular ring patch antenna loaded with a concentric pair of double negative (DNG) and double positive (DPS) materials can squeeze the resonant dimension and reduce the size of the required patch dimension by a factor of 2.4 with  $\epsilon_r = -0.5$  and  $\mu_r = -1.0$ . Other work has shown that miniaturization for a certain resonant mode, along with adequate radiation, is possible.<sup>[170–174]</sup> Loading a transmission line (TL) in a capacitively loaded resonator (CLR) and inductively loaded resonator (ILR) produced a significant size reduction since the resonant frequency depends on the LC values.<sup>[148,173,174]</sup>

Metamaterials can also improve antenna gain. Since the antenna gain is proportional to the aperture, a compact design usually reduces the gain as well as efficiency,<sup>[175]</sup> but metamaterial superstrates (a layer is placed on top of the antenna) and/or lenses can be used to actually enhance the gain while maintaining a low profile. One such approach is to use a zero refractive index metamaterial (ZIM) or near-zero refractive index metamaterial (NZIM) as a superstrate to enhance directivity and gain, reduce side-lobes and improve aperture efficiency. According to Snell’s law, as the refractive index approaches zero, the transmitted wave emerges perpendicular to the boundary surface regardless of the incident angle.<sup>[175–177]</sup> Zero or near-zero refractive index metamaterial can be fabricated from SRR (Figure 1o) or metallic square-rings with diagonal strips.

### 3. How Metamaterials have been Made So Far

PMs may offer extraordinary properties for steering light, but they’re difficult to manufacture because they demand nanometer-scale precision and registration, peculiar materials and a means for fabrication that does not necessarily scale up (at least so far). Following up on promising pioneering efforts, “top-down, layer-by-layer” strategies have been used to fabricate nanostructures by repeated application of lithography, etching, and metal deposition—stacking and arranging layers,<sup>[72]</sup> or simply using subtractive operations such as drilling into a block of dielectric material to produce PMs.<sup>[178]</sup> However, these processes are time-consuming and suffer from inconsistency especially on a scale suitable for manufacturing.<sup>[179]</sup> Likewise additive manufacturing (AM) or 3D printing can construct metamaterials with nested features and high degrees of structural complexity, layer-by-layer from meta-atoms designed in CAD, but it is a slow, serial process limited by the speed and precision of the stage, and it’s applicable to only a limited number of materials.<sup>[72,135,179,180]</sup>

### 3.1. “Top-Down.”

#### 3.1.1. Layer-by-Layer Construction of PMs (Lithography)

Several lithography techniques have been used to fabricate PMs, such as (serial) electron beam lithography (EBL),<sup>[171–174,181]</sup> focused ion beam milling (FIB),<sup>[185]</sup> nanoimprint lithography (NIL),<sup>[186,187,73,188–190]</sup> direct (laser and inkjet) writing<sup>[191–193]</sup> and photolithography (extreme ultraviolet EUV, in particular).<sup>[171,194]</sup> EBL uses a high-energy, focused electron beam to expose a resist-coated surface. The exposed resist dissolves in a developer to create a feature upon which either a metallic or dielectric layer is deposited and then, using a “lift-off” process, the resist is removed to reveal a structure as small as a few nanometers in size. EBL suffers limitations, however; among them are: low-throughput—i.e. long duration write times even with a fast (sensitive) resist; stitching errors; proximity effects; and electron beam instability that all combine to frustrate patterning a large area (economically) quickly. For all these reasons, combined with the cost of the capital equipment, EBL is problematic for large-scale production—it’s failed to be viable for fabrication of semiconductor ICs too. Other layer-by-layer technologies that are derivative of EBL have been tried including FIB milling and direct laser writing,<sup>[191,192]</sup> but suffer similar limitations such as (ion-)beam damage (FIB), and time-consuming, serial processing.<sup>[74]</sup>

On the other hand, NIL has emerged as a viable alternative due to its low cost, high throughput and the possibility of large-scale device fabrication. This method makes use of a master mold or stamp produced using other techniques (such as EBL). To transfer the topography, the stamp is pressed into a thin layer of resist that’s spun onto a substrate. The resist layer is then either cured with UV light or fixed thermally or etched into the substrate. NIL steppers can be used for volume manufacture, but patterning uneven surfaces is difficult. The main disadvantage of this technique is associated with the mold/stamp, however. Its fabrication is costly, time consuming, and it wears. Any defect in the stamp is eventually transferred to the nanostructure.<sup>[73,186–190]</sup>

Due to the demand for extremely small feature sizes, EUV- and photo-lithography have emerged as the main technology to transfer patterns in semiconductor nanofabrication.<sup>[71,194,195]</sup> The smallest feature size attainable depends critically on the mask layout, the wavelength of the exposure light,  $\lambda$ , and the numerical aperture,  $NA$ , of the optics. According to the Rayleigh equation  $CD = k_1 \lambda / NA$ , where  $CD$  denotes the critical dimension or the smallest feature and  $k_1$  is the Rayleigh coefficient. The wavelength used in photo-lithography has been squeezed down according to the demands of the semiconductor industry, starting with visible light ( $\lambda = 463$  nm) moving to ultraviolet ( $\lambda = 365$  nm) and deep ultraviolet  $\lambda = 248$  nm to  $\lambda = 193$  nm and now extreme ultra-violet,  $\lambda = 13.5$  nm.<sup>[196–198]</sup> Utilizing light at a wavelength of approximately 13.5 nm, EUV provides a solution for the limitations faced by other methods, and is actively used for manufacturing beyond the “5 nm” nodes—it is expected to satisfy the needs of the “2 nm” node.<sup>[199–201]</sup> This technology not only enables the production of advanced microprocessors and memory chips, but is also gaining traction in the field of metamaterials. EUV lithography employs a process known as laser-produced plasma (LPP) system that uses a high-power, 40–60 kW  $CO_2$  laser to irradiate  $Sn$  droplets to generate a high temperature plasma that radiates

extreme UV. The UV light then passes through a sophisticated optical system comprised of multiple-layer coated Bragg reflectors and ultimately focuses on a complex and expensive mask to transfer a pattern onto a substrate coated with a photoresist. This is all accomplished in high vacuum to reduce absorption by air. The pattern is subsequently etched into the substrate. This process can be repeated for different layers and has allowed for 3D stacking of up to 25 EUV layers in the “3 nm” node so far.<sup>[202]</sup>

EUV lithography is a high throughput technique, making it useful for high-volume manufacturing in industry by mitigating the associated costs,<sup>[203]</sup> but it suffers limitations too. One of the most severe comes from photon shot noise. Since the photon energy of the EUV is much higher, the number of photons absorbed by the resist is much lower compared to the other techniques for the same dose. This causes a statistical variation in the exposure contributing to line edge roughness (LER).<sup>[204]</sup> Mask defects impose another limitation. A EUV mask works by Bragg diffraction. It consists of alternating layers of  $Mo$  and  $Si$  capped with  $Ru$  and a  $Ta$ -based absorbing layer that is patterned over the capping layer—all deposited onto a glass substrate. Masks are so expensive to begin with,<sup>[204–206]</sup> and that cost is compounded by the lack of a pellicle. A pellicle is a thin, transparent membrane that is used to protect the mask from contamination and damage during lithography, but one does not yet exist for EUV<sup>[204]</sup> and so, defects and contamination of the mask significantly impacts the production yield as well as the cost. Finally, the “killer” limitations are the initial capital outlay: \$380 million for a high-NA Advanced Semiconductor Materials Lithography (ASML) EUV lithography tool along with the high cost of maintenance (which is about 5% annually of the initial cost of the tool).

#### 3.1.2. Layer-by-Layer Construction of PMs (Etch and Deposition)

Along with lithography, “top-down, layer-by-layer” fabrication of a metamaterial also entails complex deposition and either removal techniques such as “lift-off” or etching. Creating nanometer-scale features this way implies nanometer-scale etch resolution and high anisotropy in the etch direction. This is accomplished using both dry and wet etching techniques. The etching speed can be improved by employing chemical and physical dry etching together such as in reactive ion etching (RIE).

This is how RIE works. A gas glow discharge is used to dissociate and ionize a relatively stable molecule (like  $SF_6$  used for etching silicon) into a chemically reactive species. The substrate is positioned on a radio frequency (RF)-driven, capacitive-coupled electrode. Once the plasma is ignited, due to the higher mobility of the electrons compared to the ions, the substrate becomes negatively charged. The reactive intermediates that are generated in the glow chamber are then transported to the substrate surface from the bulk of the plasma through diffusion and the positive ions from the glow region are driven to the surface through the DC self-bias acquired by the substrate. The reactive species are absorbed by the substrate and react with it to produce volatile products that are subsequently purged. RIE usually creates 2D structures through an etch mask formed by lithography using a vertical etching process. However, when combined with angled chemical etching it can generate 3D structures as well.<sup>[207–209]</sup> High quality, 3D optical nanocavities were created this way inside

a single diamond crystal using (inductively coupled plasma)–RIE in which the angle etching was done in a Faraday cage.<sup>[208,209]</sup> In another example, 3D photonic crystals were created in single crystal silicon wafer.<sup>[207]</sup> RIE in combination with the soft imprint lithography (SNL) has been used to fabricate tunable dielectric or metallic meta-surfaces<sup>[190]</sup> and a coaxial plasmonic metamaterial was fabricated using a combination of EBL and RIE.<sup>[210]</sup>

RIE has the advantage that the etching process is anisotropic, which develops from the energetic ions and the directionality of the ion bombardment. This is useful for etching high-aspect ratio structures, allowing almost vertical trenches unlike chemical etching, which for homogeneous substrates causes a spherical groove.<sup>[211,212]</sup> RIE is also a high-throughput, batch process making it suitable for volume manufacturing. With these advantages, this method is used prevalently in IC manufacturing.<sup>[213,214]</sup> The drawback with RIE is substrate damage. The physical bombardment of the high energy ions can cause lattice damage in the underlying substrate, which increases the surface roughness of the substrate and can be electrically active.<sup>[214]</sup> Other problems include etch lag, which refers to an etching rate that is smaller for the smaller size features than that of the larger size features. Generally, larger size features etch faster than smaller size features causing unequal etch depths across the wafer and so, in order to complete the etching of smaller size features, the larger features are over etched resulting in a loss of dimensional control, and aspect ratio dependent etching (ARDE), which refers to the change in the aspect ratio increases due to the limited diffusion to the bottom of a feature.

Complementary to etch, deposition techniques such as chemical vapor deposition (CVD), physical vapor deposition (PVD) techniques and atomic layer deposition (ALD) likely figure into metamaterial fabrication as well. A CVD process typically involves the introduction of a volatile precursor into the reaction chamber where it decomposes after interaction with the substrate depositing various materials. This is typically used in combination with patterning and templating. For example, direct 3D structures have been produced in which carbon nanotube (CNT)-based features were deposited using CVD. The growth rate of the CNT structures depends on the underlying catalyst. Patterning the catalyst on the substrate layer can cause bending that creates curved structures.<sup>[215]</sup> Glancing angle deposition (GLAD) is a PVD process that can also be used to create 3D nanostructures.<sup>[216–218]</sup> In a PVD process the stream of vapor-phase atoms strike the substrate in a perpendicular direction and condense on it forming a film. On the other hand, in GLAD the atoms strike at a glancing angle with respect to the substrate surface. The atoms spontaneously nucleate to create a shadow against the atomic trajectory, preventing deposition against it, and affecting the development of columns tilted toward the source. By rotating the substrate 3D structures with different sources can be created this way.

ALD is a thin film deposition technique in which chemical precursors are alternatively applied to a substrate surface that chemically react with the surface to form an atomically thin layer. Due to the self-limiting growth, precise thickness control and excellent deposition quality, ALD is widely employed especially due to the increased demand for miniaturization of semiconductor devices. No other deposition technique has achieved a similar level of control or conformality.<sup>[219–232]</sup> ALD is distinguished from CVD in

the method by which the precursors are introduced in the chamber. In CVD the precursors are pumped simultaneously into the chamber, allowing them to react and form a thin film on the surface whereas ALD uses a sequential method in which each precursor is pumped into the chamber in pulses one at a time.<sup>[223,224]</sup> The sequential pulsing offers precise control over the chemical reaction on the substrate surface. After the introduction, the first precursor reacts with the substrate and forms a monolayer, the chamber is then purged to remove any excess precursor and any by-products. Then the second precursor is introduced and reacts with the first layer. The chamber is purged again, and the process is repeated several times to reach a specified thickness. This cyclic method ensures that each layer is deposited with an atomic precision. An ultra-thin film with exceptional uniformity and conformity can be produced this way. The self-limiting nature of the reaction is the key to ALD. The reaction of the first precursor with the substrate is only possible until the substrate surface is completely saturated with the precursor molecule, which is subsequently purged so that no further reaction between the first precursor molecule and another precursor is possible.

The architecture of a metamaterial involves an intricate arrangement and composition of the constituent elements and so, ALD can play a pivotal role in the fabrication. For example, ALD was used to deposit alternate layers of  $ZnO/Al_2O_3$  with different thicknesses by changing the ALD cycles for  $ZnO$  and  $Al_2O_3$  at a 9:1 ratio to create a metamaterial with hyperbolic dispersion in the near infrared.<sup>[225]</sup> A similar application of ALD was used to create a nonlinear optical metamaterial by alternatively depositing three layers of transparent amorphous materials ( $TiO_2$ ,  $Al_2O_3$ , and  $In_2O_3$ ) and then repeating the structure according to the design thickness.<sup>[226]</sup> Likewise, an epsilon-near-zero (ENZ) metamaterial was created using the ALD by alternatively depositing  $Ir/Al_2O_3$  and varying the corresponding deposition cycle.<sup>[227]</sup> Thus, ALD features atomic-scale control over the thickness of the deposited material and can grow high quality ultra-thin films at relatively low temperatures (even below 100 °C) compared to other deposition processes.<sup>[225–230]</sup> On the other hand, ALD is a time-consuming process. Layer-by-layer deposition is generally slower than other deposition methods such as CVD, especially for thick film deposition.<sup>[231]</sup> Another disadvantage is the high operating cost. Almost 60% of the precursor is wasted in the process.<sup>[231,232]</sup>

### 3.1.3. 3D Additive Manufacturing (AM) of PMs

“Top-down” approaches to the fabrication of metamaterials include holographic lithography, also known as interference lithography. Holographic lithography involves the generation of a 3D interference pattern by superimposing coherent light waves to expose a photo-sensitive material.<sup>[233–236]</sup> By adjusting the angle and polarization of the laser beams, various nanostructures can be created using this process with feature sizes as small as 10 nm.<sup>[237]</sup> The resulting 3D structure can then serve as a template for integration of even more functionality. This method can create a wide variety of periodic and semi-periodic 3D structures such as “woodpile” structures (Figure 1i) or quasi-crystal systems.

Other optical techniques such as multi-photon polymerization (MPP) use a scanning beam to create 3D structures with

practically arbitrary shapes and sizes.<sup>[238–240]</sup> MPP starts off by patterning a photosensitive material using a mask to form features that can then be used to create structures in other materials such as metal or ceramic by conformal deposition and selective removal of the polymer. MPP has been used this way to fabricate complex, free-standing structures with sub-micron feature sizes that mimic a crystal lattice. The process latitude that MPP brings with it to the fabrication of metamaterials is obvious from structures like chiral PMs that are much more difficult to produce with conventional methods (Figure 1e,f,j).

However, according to Askari *et al.*,<sup>[72]</sup> MPP has a speed limit and a limited field of view due to the high NA objective lens that restrict the applications. For example, to fabricate millimeter-sized structures, a MPP system would have to use a high-speed laser scanning system accompanied by a piezoelectric stage for precise alignment. In addition, following Bourell,<sup>[180]</sup> the feedstock has to be compatible with the process. For example, in vat polymerization used for 3D printing, liquid polymeric inks are selectively cured layer-by-layer. The feedstock has to be a liquid thermoset plastic monomer that crosslinks when it is exposed to UV light form plastic. Moreover, according to Askari *et al.*<sup>[72]</sup> the difference in refractive index between commercial MPP resins and air is not usually wide enough to accommodate a complete photonic bandgap; it has to be 1.9 to produce a stop-band.<sup>[241,15]</sup> There are several approaches to resolving the bandgap problem. One is to use customized resins with a high dielectric constant;<sup>[197]</sup> another is to use  $As_2S_3$  chalcogenide glass in which a thin film is deposited on the substrate using thermal vapor deposition. Utilizing the high refractive index of  $As_2S_3$  (2.45–2.53), MPP was used to fabricate a photonic bandgap (PBG) material with a 3.5% gap per mid-gap ratio.<sup>[231]</sup>

## 3.2. “Bottom-Up.”

### 3.2.1. 3D Self-Assembly of PMs

Self-assembly (SA) is just the opposite of the “top-down” techniques used to fabricate metamaterials. SA refers to the process by which the discrete components such as atoms or nanoparticles are organized by a local interaction between the components and the environment to establish long range order.<sup>[242–244]</sup> The impelling force is the reduction of free energy toward a local thermodynamic equilibrium, which can be accomplished directly by the inter-particle forces or indirectly through an external field or template.<sup>[44,244–246]</sup> Specifically, metamaterials have been assembled by using block co-polymers, colloidal chemistry or by strain engineering using martensitic phase transformations or by “binding” in an intense optical field.

### 3.2.2. Block Co-Polymer Self-Assembly

A block co-polymer (BCP) is a type of macromolecule synthesized from two or more homopolymers covalently linked together. Each block is made from different, thermodynamically incompatible monomers that are covalently bonded to produce micro- or nanostructures. The structures can then be used as templates for nanolithography to produce nano- or micro-scale

structures that constitute a metamaterial or not. For example, a 3D optical metamaterial with unit cell 50 nm in size was created based on BCP self-assembly by using an isoprene-block-styrene-block-ethylene oxide (ISO-) BCP to create an interpenetrating gyroid network (i.e. triply periodic network with minimal surface), one in which the (isoprene) network was then removed by UV treatment and chemical etching and subsequently backfilled with gold by electrodeposition. The rest of the structure was then removed to produce a continuous triply periodic gold structure that exhibited anisotropic plasmon modes in the visible region.<sup>[247]</sup>

### 3.2.3. Colloidal Crystal Self-Assembly

Colloidal SA is yet another approach to fabricating metamaterials.<sup>86,244,248–250</sup> For example, a raspberry-like structure was created using negatively charged silica NPs that self-assembled into a bulk metamaterial that exhibited strong isotropic optical magnetism in the visible.<sup>[244]</sup> In another example, a skin-like soft metamaterial was produced using NPs formed from hollow pillars. The hollow pillars were first produced by the SA of 10 nm Au NPs that were then arranged vertically on a macro-scale gold film. This metamaterial could be used as dual-band camouflage both in the visible and infrared.<sup>[248]</sup> In this work a double-fishnet, negative refractive index metamaterial was created from a hexagonal array of holes on a gold-silica-gold layer stack. The hexagonal arrays were created by using a self-assembled close packed monolayer of polystyrene beads and NP (spherical) lithography. An unnaturally high refractive index optical metamaterial was created this way using the interfacial self-assembly between oil (hexane) and aqueous colloidal suspension of gold nanocrystals.<sup>[86,250]</sup>

### 3.2.4. Martensitic Phase Transformations

Martensitic phase transformations offer a novel approach to the fabrication of meta-surfaces.<sup>[3]</sup> A martensitic transformation is a solid-to-solid phase transition that occurs between a high-symmetry and a low-symmetry crystallographic phases without changing the chemical composition. Each phase can have distinct optical properties, for example, but usually the two phases are structurally incompatible resulting in internal strain. The low-symmetry phase usually forms twins to accommodate the strain. The trick that Prakash *et al.*<sup>[3]</sup> use is thin 2D films in which the out-of-plane direction is free and so the requirement for kinematic compatibility is relaxed. With this trick, they show it's possible to produce a thin film of perovskite  $SrSnO_3$  with reconfigurable periodic nanostructures consisting of regularly spaced regions of sharply contrasting dielectric properties (Figure 1a). Thus, the dielectric constant of the film can be tuned to create a variable photonic crystal.

### 3.2.5. Optical Binding

Optical binding uses a uniform laser beam to form self-organized, photonic crystals through light-mediated inter-particle interactions, derived from the mutual Lorentz force that

redistributes the momentum in the incident beam.<sup>[44,251]</sup> (This differs, in principle and in practice, from how light gradients are used to assemble nanoparticles).<sup>[10]</sup> Importantly, the time-averaged Lorentz force decreases with distance  $r$  like  $1/r^4$  in the near-field and  $1/r$  in the far-field. Optical binding is strong. It depends on the particle size, the material and the light intensity and polarization, and the resulting force ranges from 1  $\mu$ N to 1 nN. For a distance comparable to the wavelength, the mutual Lorentz force on 100 nm-radius Au NPs in water is supposed to be  $\approx$  20-fold stronger than the light-gradient force at the peak intensity in a 70 mW Gaussian beam.<sup>[121]</sup> Although optical binding can be stronger apparently than the gradient force in an intense field, “optical matter” formed this way is nevertheless constrained in size, shape, constituency and inter-particle spacing.<sup>[44]</sup> (On the other hand, the constraints on light gradient forces are associated mainly with distortions in the electromagnetic environment encountered during assembly, which restricts the packing density of NPs that is set by  $\lambda$ , the laser wavelength, to  $\lambda/2$ —the separation between anti-nodes/nodes in a standing wave. To compensate for these distortions, one work-around that is exploited here is a so-called “diffraction-free,” self-reconstructing Bessel beam).<sup>[10]</sup>

#### 4. Combining “Top-Down” and “Bottom-Up” Methods to Manufacture PMs

The use of light gradient forces to manipulate and organize nanometer-scale matter is a radically different strategy for manufacturing metamaterials. Although it has proven feasible to manipulate atoms such as Na,<sup>[90]</sup> Cr,<sup>[91–93]</sup> and Al,<sup>[94]</sup> and molecules,<sup>[95,96]</sup> constructing a heterogeneous metamaterial up from atoms and molecules this way is impractical right now because of the limited throughput defined by the optical absorption of the atomic beam, which has to be minimized to maintain the optical trap, and the corresponding scale of the irradiance and the positional stability required.<sup>[90]</sup> On the other hand, using light to manipulate nanoparticles has proven feasible.<sup>[10]</sup> If a particle is small enough, i.e.  $< \lambda/20$ , where  $\lambda$  is the wavelength of light, then it can be treated as a simple, induced point dipole interacting with the optical field according to the theory of Rayleigh scattering. Two types of forces develop as a result: the scattering force due to changes in electromagnetic momentum associated with scattering from the dipole, which is directed along the incident light beam; and the gradient force, which is just the Lorentz force acting on the induced dipole directed toward the center of the beam (if the index of the particle exceeds the index of the medium).

##### 4.1. Optical Trapping

A single-beam optical trap, also called an “optical tweezers”, is the simplest implementation and it’s used prevalently. It is produced by focusing a  $TEM_{00}$  laser beam of wavelength  $\lambda$  to the diffraction-limit with a high NA microscope objective (Figure 7). This is usually accomplished with a commercial, high-resolution optical microscope in which the same objective is used for viewing and to focus a laser beam for trapping. The single beam trap was originally designed for use in the Rayleigh scattering limit, but subsequently, it has been used on much (Mie) larger particles. Assuming that the force  $F \approx \kappa x$ , the stiffness,  $\kappa$ , that results is found to increase about linearly with laser power and

with the refractive index mismatch between the particle and the medium, reaching a maximum at particle radius of  $\approx$  500 nm before decreasing with increasing radius. Simmons,<sup>[103]</sup> Tlusty<sup>[106]</sup> and others<sup>[107]</sup> have interpreted this observation as evidence of the  $a^3$ -increase predicted by dipole theory and  $a^{-1}$ -decrease expected from geometric optics.<sup>[116]</sup>

Following Paul *et al.*<sup>[10]</sup> the strength of the trapping force depends on the topography of the optical field and on the properties of the particle and surrounding medium. For a Gaussian beam (in the paraxial approximation), the intensity  $I(r)$  is:

$$I(\vec{r}) = \frac{2P \cdot \pi \cdot n_m}{\pi \cdot w^2(z)} \cdot \exp[-2r^2/w(z)^2] \quad (2)$$

where:

$$w^2(z) = w_0^2(z) \cdot [1 + (z/z_0)^2] \quad (3)$$

and  $z_0 = \pi w_0^2/\lambda$ , where  $w_0$  is the beam waist in the focal plane,  $P$  is the laser power, and  $n_m$  is the medium index and the corresponding (gradient) force on a NP of radius  $a$  is given by:

$$\vec{F}_{grad}(\vec{r}) = \frac{2\pi \cdot n_m}{c} a^3 \left( \frac{m^2 - 1}{m^2 + 2} \right)^2 \nabla I(\vec{r}) \quad (4)$$

where  $m$  denotes the ratio of the NP index to the medium index, i.e.  $m = n_{NP}/n_m$ , which scales like  $\approx (n_{NP} - n_m) a^3$ . Therefore, following Barelett and Henderson,<sup>[115]</sup> the stiffness in the lateral direction, defined by  $\kappa_r = -\partial(\hat{x} \cdot \vec{F}_{grad})/\partial x$ , is:

$$\kappa_r = \frac{32P}{3w_0^4 c} a^3 (n_p - n_m) \quad (5)$$

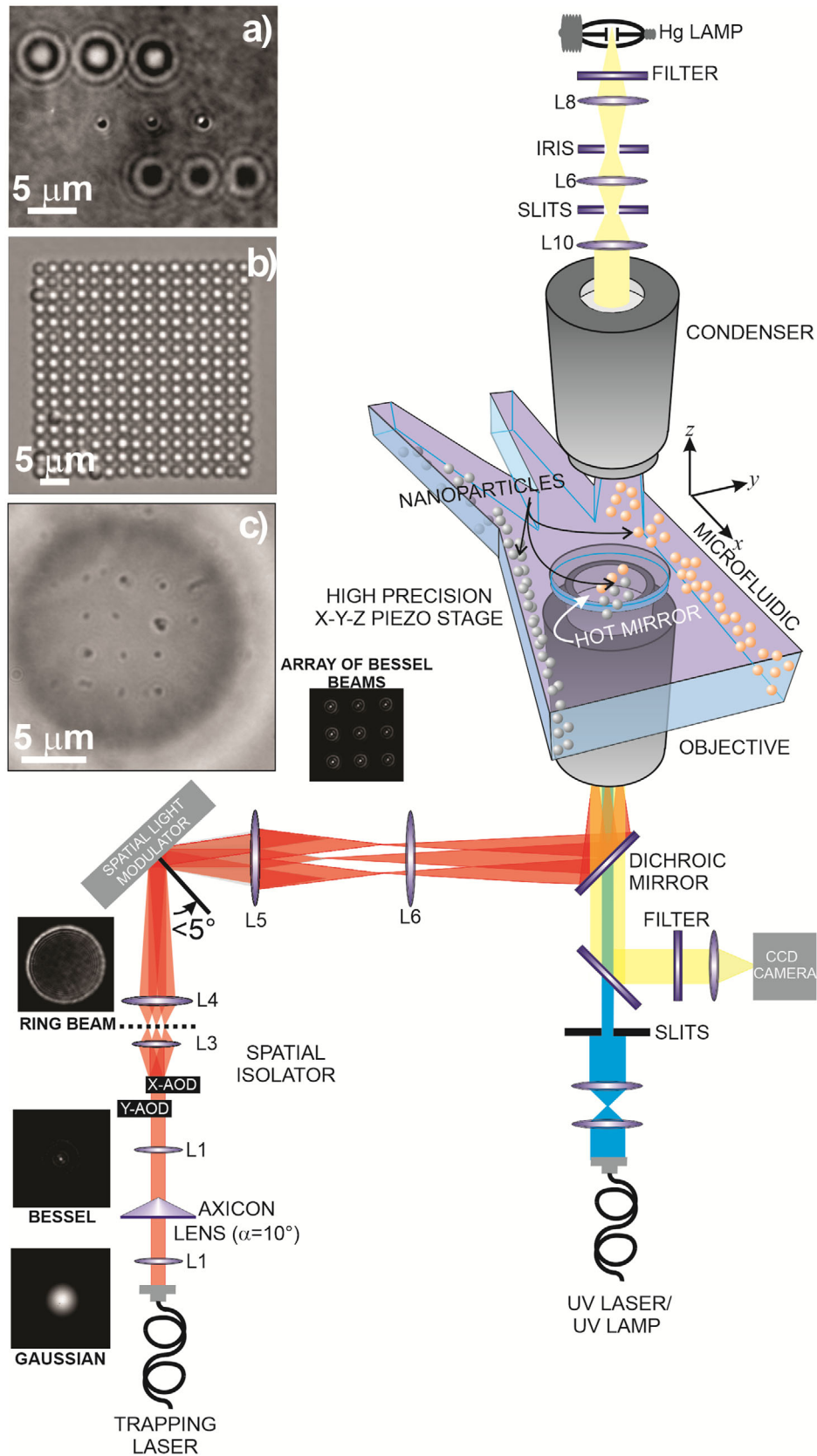
so that for a silica particle with  $a = 50$  nm,  $P = 1.5$  W,  $\kappa_r < 0.5$  pN per nm, typically. According to this analysis, the forces that produce a stable trap result in a potential well that is deep enough to overcome the kinetic energy associated with Brownian motion. This condition on the potential can be expressed as follows:<sup>[115]</sup> from which an estimate for the minimum particle size that can be trapped using a single-beam focused to the diffraction limit can be derived: i.e.

At room temperature, for a silica sphere in water with  $m = 1.65/1.33 = 1.24$ ,  $2w_0 = 1.5\lambda = 0.58 \mu$ m, and  $P = 1.5$  W, the minimum particle diameter is about  $2a = 19$  nm.

$$U = \frac{2\pi \cdot n_m a^3}{c} \left( \frac{m^2 - 1}{m^2 + 2} \right) \frac{P}{\pi w_0^2} \geq 10k_B T \quad (6)$$

$$a^3 \geq \frac{5k_B T \cdot c w_0^2}{2 \cdot n_m \cdot P} \left( \frac{m^2 + 2}{m^2 - 1} \right) \quad (7)$$

The relatively large size of the minimum particle that results from this analysis develops from the weak confinement along the axial direction. The axial confinement can be improved dramatically by using a standing wave optical trap (SWOT) instead of a single beam, i.e. reflecting the laser beam back onto itself. The formation of a Gaussian standing wave has the effect of localizing dielectric NPs in the anti-nodes of the standing wave. Since the anti-nodes are separated by only  $\lambda/2$ , there is an increase in the



intensity gradient, and therefore an order of magnitude increase in the stiffness. Using the same criteria as above, the minimum particle size that can be trapped using a SWOT is given by:<sup>[114,115]</sup>

$$a^3 \geq \frac{5k_B T \cdot cw_0^2}{2n_m \cdot P} \left( \frac{m^2 + 2}{m^2 - 1} \right) \frac{1}{(1 + \rho)^2} \quad (8)$$

where  $\rho$  is the absolute value of the reflection coefficient. If  $\rho = 1$ , then  $a$  is a factor of  $\approx 1.6$  smaller or a NP of diameter  $2a = 12$  nm. And so, we find that NPs with  $2a \approx 10$ – $50$  nm diameter can be effectively trapped using light, but only with high power.

Based on this analysis, to manufacture a PM using light gradients, precisely formed NPs have to be assembled with enough registration to avoid losses due to scattering and the process for manufacturing the NPs has to be scalable. To that end, several technical problems have to be resolved. Following Paul *et al.*,<sup>[10]</sup> **First**, the sensitivity of the trap to the size and optical properties of the particle means that the “bottom-up” synthesis of the NPs has to produce monodispersed particles with high yield with a CV  $\leq 1\%$ . **Second**, whereas a NP doesn't weigh much, light gradient forces top out at  $\approx 100$  pN –  $1$  nN. That, combined with buoyancy and Stoke's flow (in liquid) around the particle constrains the minimum laser power. On the other hand, the maximum laser power is affected by the two-photon effects (the bandgap of the NP material), heating and melting (of reflectionless, coated) optics. **Third**, doubtless one trap is not enough. For high-throughput, multiple traps will have to be implemented concurrently, which places another constraint on the minimum power. **Fourth**, although optical trapping can create complex heterogeneous arrays of NPs, the light still has to be held on them to maintain the array, which affects the maximum size and number of NPs in a voxel unless a scaffold is used to fix the NP positions. To relax the power specification and, at the same time, improve the throughput, the manufacture of a heterogeneous metamaterial can be divided into four separate tasks: the synthesis of NPs, CAD, the assembly of them using light and vitrification. One implementation that addresses all of the constraints is tersely described below.<sup>[10]</sup>

#### 4.2. Nanoparticle Synthesis

Nanoparticles can form the building blocks for metamaterials and light can be the glue that holds them together (at least temporarily). According to the analysis of how an optical trap works, the size and constituency of the NP plays a crucial role in optical trapping. Irregularities in the size or index of the NPs constituting a metamaterial lead to variations in phase delay (Figure 6), the trap potential,  $U$ , and therefore, increased (spatial) noise

and random scattering that can have a detrimental effect on performance. NPs can be synthesized precisely either by “top-down” decomposition, sputtering or milling of bulk materials or by ‘bottom-up’ methods that nucleate and grow particles from fine molecular distributions in liquid or vapor phase, including functionalization by conjugation, for example.<sup>[252,253]</sup> On the one hand, “top-down” methods (like lithography and etching) can yield narrow particle and shape distributions suitable for optical trapping, but similar to a silicon ICs, it is expensive to fabricate them that way. On the other hand, high yield can be recovered from the “bottom-up” approaches like liquid-phase and vapor-phase synthesis, which makes them more economical and green (environmentally friendly).

These “bottom-up” processes can be categorized as liquid-phase synthesis<sup>[254]</sup> that include precipitation,<sup>[255–258]</sup> hydro-thermal synthesis,<sup>[259–263]</sup> sol-gel fabrication<sup>[264,265]</sup> and microemulsions.<sup>[266–269]</sup> Liquid phase synthesis of NPs, starts from soluble precursors that produces species in a super-saturated state after chemical reactions, eventually causing nucleation that produces NPs. Liquid phase methods can offer control over the shape and size of a NP<sup>[259–263]</sup> and can produce stable dispersions, but not always.<sup>[255–258]</sup> The aggregation of the particles produced this way can be avoided by using ligands or surfactants.<sup>[270]</sup> Sol-gel and microemulsion are the easiest and most affordable methods used to synthesize nanoparticles; their big advantages are that they can be performed in low temperature, and provide exceptional control over the size of the particle producing nanoparticles with a very narrow size distribution.<sup>[264,265]</sup>

Unlike liquid-phase synthesis, vapor-phase synthesis, which includes pyrolysis<sup>[270–274]</sup> and inert gas condensation,<sup>[275–278]</sup> starts from gaseous precursors. The precursors are delivered either as a gas or as small droplets that are vaporized in the process. Vapors are generally produced from precursor materials typically available in solid or liquid form using different techniques such as thermal evaporation, laser ablation, sputtering or high-voltage spark. The vapor is then mixed with a beam of inert gas such as argon (*Ar*) to transport it to a chamber where the condensation occurs. The mixture must be super-saturated in order for condensation to occur. The mixture can also take the form of chemical super-saturation, in which vapor molecules react chemically to form the condensed phase. If the super-saturation level is sufficient, nucleation happens homogeneously. After nucleation, the degree of super-saturation is reduced and the particles enter in a growth phase instead. In order to create smaller particles, a high degree of super-saturation is used to generate more nucleation, and then the system is quenched immediately to stop the growth. Particle sizes as small as a few nanometers can be produced this way and the size distribution can be tightly controlled. For example, *Au-Pd* NPs with a mean diameter of only 5 nm have been

**Figure 7.** Time-shared and holographic optical trapping apparatus and microfluidic conveyer. Nanoparticles are manipulated using optical traps formed with an infrared laser (red) and detected through a microscope. The evolution of the trapping beam profile from a Gaussian to a quasi-Bessel beam is delineated by the intensity maps located alongside the red IR-laser track in the figure. The microscope optics can also be used for (fluorescent) imaging (yellow path). a) An optical micrograph a 3D- $3 \times 3 \times 3$  array produced using the acousto-optic deflectors (AODs) in combination with the spatial light modulator (SLM). In the transmission image, the center row is in focus, while the upper and lower rows are over and under focused respectively. b) A transmission optical micrograph of a 2D- $16 \times 16$  array of 500 nm diameter NPs is shown. c) A transmission optical micrograph of a 2D- $4 \times 4$  array of 1:50 ( $\text{SiO}_2$ -*Au*) 500 nm-diameter core-shell NPs formed using a time-shared array of Gaussian optical traps at  $\lambda = 1064$  nm with irradiance of 230 mW and photopolymerized on a hydrogel scaffold. Adapted from ref. [10].

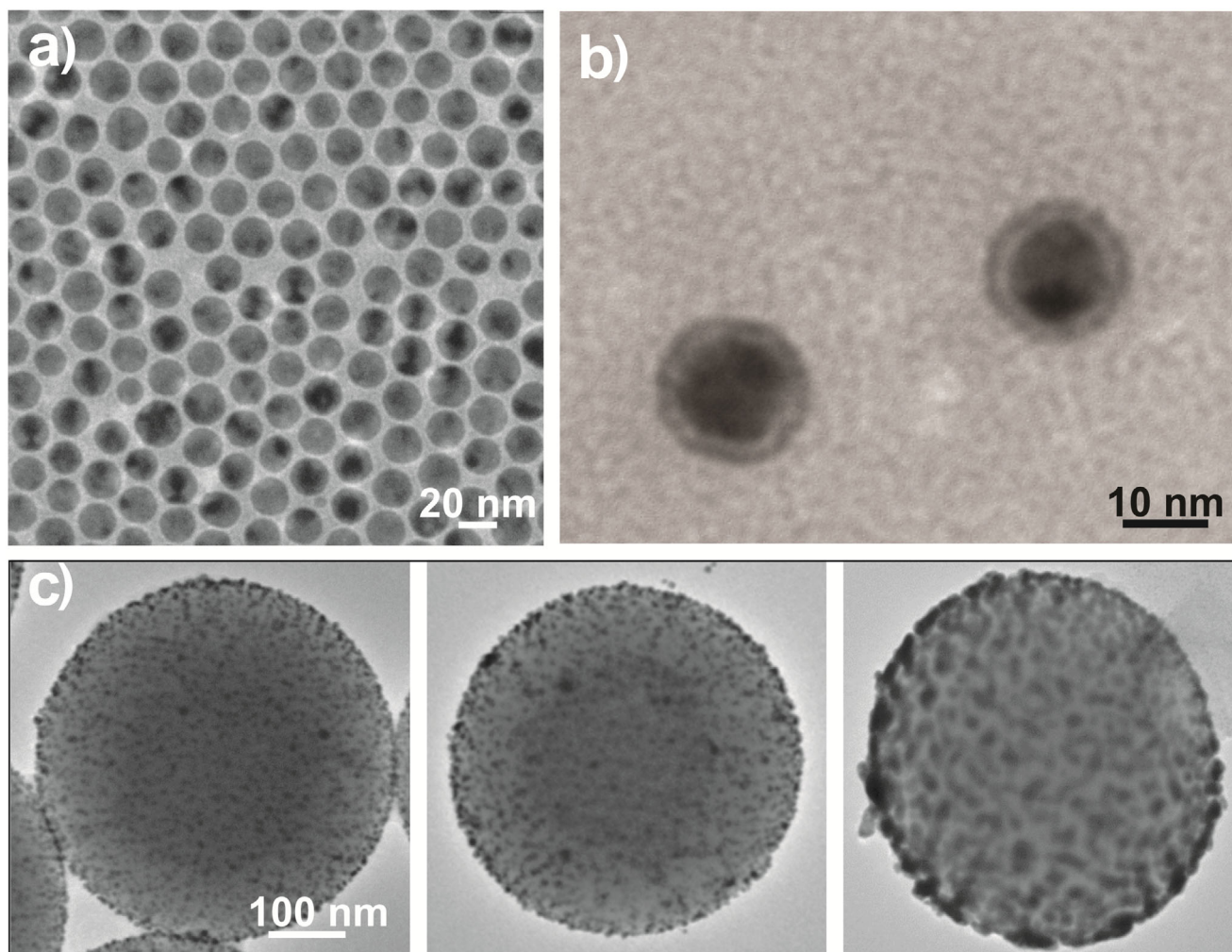


**Figure 8.** NP ‘bottom-up’ synthesis. a) A transmission electron micrograph (TEM) is shown of monodispersed (diameter  $16.2 \pm 2.3$  nm) Au NPs prepared by oleylamine reduction. b) A TEM is shown of Au-core, silica-shell (Au@silica) NPs with a shell thickness that was stringently controlled through the *igepal* MW and the concentration of TEOS used in the synthesis. c) Synthesis of silica@Au core-shell NPs with a tunable surface density of the Au shell. TEM micrographs show (left to right) silica@Au core-shell NPs prepared using a volumetric of silica core NPs and Au seed NPs of 1:10 (left) 1:50 (center), and 1:100 (right) prior to plating, which resulted in a tunable surface density of Au. Adapted from ref. [265].

synthesized with a standard deviation of only 0.07 nm.<sup>[277]</sup> Another advantage of the vapor phase method is the purity, since the process does not involve any liquid solution. This process is also much faster compared to liquid-phase synthesis and can be scaled up to volume production. However, the coagulation and coalescence of the NPs produced this way is a drawback.

The same technologies that produce such stringent control of NP size, shape and distribution are not confined to simply homogeneous (solid throughout) compositions. Heterogeneous core-shell composites with solid shells encasing either another solid, liquid or gas can now be synthesized with size-dependent and shell-dependent optical, mechanical, electronic, and chemical properties that open wide a window to a whole new range of applications (Figure 8).<sup>[265,279,280]</sup> Regarding PMs specifically, a key advantage of the core-shell NP is that optical properties such as the refractive index, absorption, etc. of the material constituting the core and shell can be tuned, which allows for precise light scattering, effectively enhancing and extending the functional-

ity of the metamaterial.<sup>[281]</sup> For example, using the core-shell NP with a Au-core and a SiO<sub>2</sub> shell (Au@SiO<sub>2</sub>), Zhang *et al.*<sup>[282]</sup> demonstrated that a self-assembled array with four layers of NPs shows near perfect (99% at  $\lambda = 537$  nm) absorption.

Core-shell NPs like this can be synthesized starting with Au. NPs can be synthesized from Au with a relatively narrow size distribution ( $16.2 \pm 2.3$  nm) using an oleylamine reduction in aqueous solution (Figure 8a). Then, starting with a Au-core, a composite core-shell (Au@SiO<sub>2</sub>) NPs can be fabricated with a SiO<sub>2</sub>-shell that has a tunable thickness, controlled by the molecular weight of the non-ionic surfactant, *igepal*, and the concentration of TEOS (Figure 8b). Conversely, an inside-out structure (SiO<sub>2</sub>@Au) can also be synthesized. Starting with monodispersed SiO<sub>2</sub> NPs with a mean diameter of 500 nm and a CV < 1% prepared using the Stöber method,<sup>[283,284]</sup> NPs with a silica core and a Au-shell were synthesized by first silanizing the silica surface with 3-amino-propyl-tri-ethoxy-silane (APTES) to produce a positive surface charge and then, absorbing negatively charged Au NP seeds

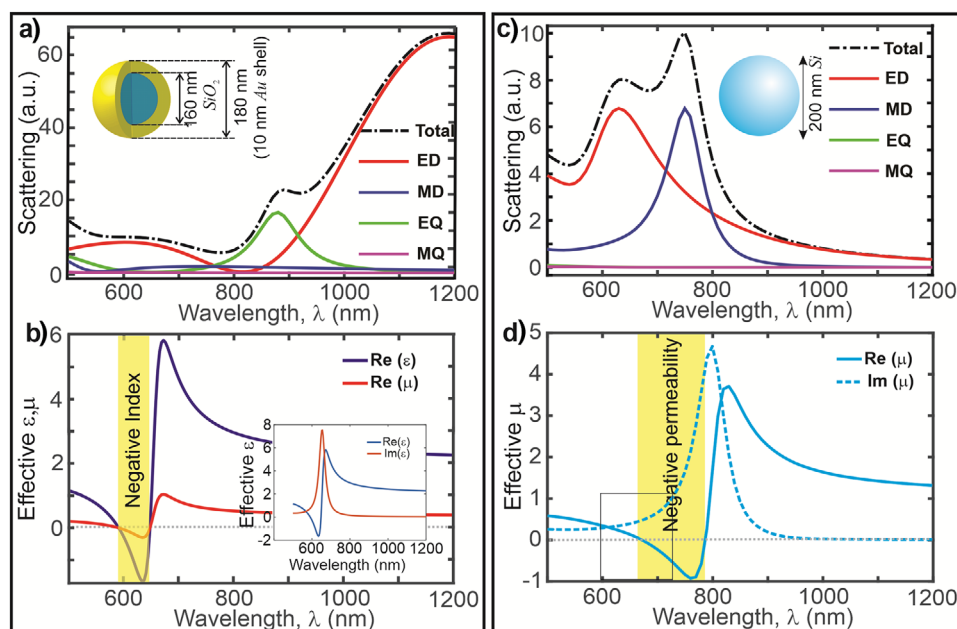


**Figure 9.** Nanoparticle dielectric response. a) Calculated optical scattering from a single 180 nm-diameter core-shell NP is shown as a function of the wavelength. The silica core, which is 160 nm in diameter, is encapsulated by a 10 nm Au shell. The total scattering (dashed-dotted line) is resolved into the electric dipole (ED, red), magnetic dipole (MD, blue), electric quadrupole (EQ, green), and magnetic quadrupole (MQ, purple) components. The higher order poles were not included. b) The recovered effective permeability and permittivity is shown as a function of the wavelength for the same NP in (a). The calculation indicates a negative index of refraction near a wavelength of  $\lambda = 630$  nm. The inset resolves the real and imaginary components of the permittivity. c) Like (a), but for a 200 nm diameter homogenous Si NP. d) The real and imaginary components of the permeability are shown for the NP in (c). Unlike the core-shell NP, the permeability is negative for the Si NP near a wavelength of  $\lambda = 730$  nm, but not the permittivity.

$\approx 5$  nm in diameter prepared by the reduction of chloroauric acid with tetrakis (hydroxymethyl) phosphonium chloride onto them.<sup>[253]</sup> A tunable surface density of Au seeds on the SiO<sub>2</sub> core was achieved by controlling the SiO<sub>2</sub>:Au mass ratio (Figure 8c). Finally, a Au-shell was grown by adding SiO<sub>2</sub>@Au core-seed NPs to a Au-plating solution.<sup>[279]</sup>

### 4.3. CAD/Simulation

Metamaterials are complex and expensive to manufacture. The “emergent” properties that develop from interactions between the constituents can be different from the separate parts. Thus, the design is critical to the emergent performance. The computational tools<sup>[285–287]</sup> used in the design of metamaterials include finite element analysis (FEA) software such as COMSOL Multi-physics, ST Microwave Studio, Ansys HFSS, and finite difference time-domain (FDTD) modeling. Topology optimization algorithms have also been used to iteratively vary the material distribution in a design and machine learning figures into this for predicting optimal configurations. As an illustration, consider how a NP that is much smaller than the incident light behaves in detail. Generally, it looks like an electric dipole and the scattering from it can be controlled by the size (Figure 9). The first Mie scattering resonance occurs near  $d n_{NP}/\lambda_0 = (m + 1)/2$ , where  $n_{NP}$  is the refractive index,  $d$  is the diameter of the NP, and  $\lambda$  denotes the free-space wavelength. When  $m = 1$ , it’s a magnetic dipole mode. The second ( $m = 2$ ) resonance is an electric dipole resonance.<sup>[61]</sup> So, to work in the visible, the diameter of the NP

must be  $d < 500$  nm, depending on the index; typically,  $\lambda_0/d > 10$ . Figure 9 shows the results of two COMSOL calculations illustrating these effects—one for a 180 nm-diameter core-shell NP (SiO<sub>2</sub>@Au) constructed with an inner core and outer shell of a different material that either fully or at least partially encapsulates the core, and another for a homogenous 200 nm-diameter Si NP. These calculations use Mie scattering theory to estimate the effective permittivity and permeability of a PM.

The electric and magnetic dipole scattering resonances associated with the core-shell NP (Figure 9a) produce a negative refractive index (Figure 9b) near a wavelength of 630 nm for a 3D PM cubic lattice where only 35% of the total volume was occupied by NPs with air as the background medium. Although 3D isotropic, negative index PMs have been produced at GHz frequencies (where the spheres were millimeter in diameter),<sup>[61]</sup> this calculation shows that the same thing could be accomplished at optical frequencies. Likewise, Mie scattering from the Si NP (Figure 9c) also produced a negative permeability in the same wavelength range (Figure 9d). Due to the absence of magnetic charges—that’s hard to do. Pendry developed a metal SRR that accomplishes the same end,<sup>[21]</sup> but a semiconductor NP was used in this calculation instead. In the near-field where electrostatics and magnetostatics apply, a superlens could be constructed with a negative permeability alone. On the other hand, instead of using just one size, a PM consisting of a heterogeneous array of Si NPs with the same refractive index but with different sizes—one NP that produces an electric dipole resonance and another producing a magnetic resonance at the same wavelength—will give rise to a negative  $\epsilon$  and  $\mu$  or a negative index of refraction. The

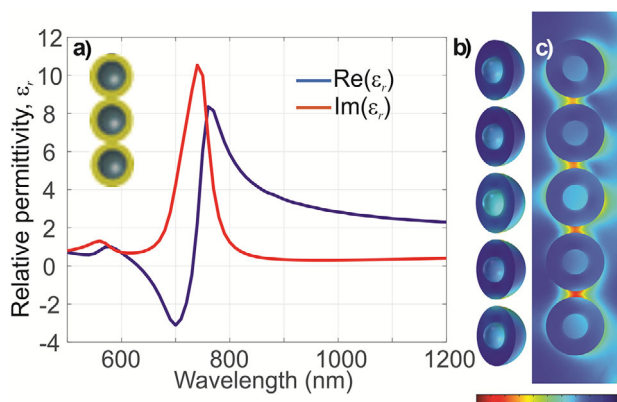


**Figure 10.** EM scattering from a core-shell NP. a) Calculated real (blue) and imaginary (red) components of the effective permittivity for 3 abutted core-shell NPs in a linear chain (shown in the upper left inset). The core is 30 nm in diameter and the shell is 20 nm thick. b) A heat-map of the magnitude of the total electric field inside  $\text{SiO}_2/\text{Au}$  core-shell NPs is shown superimposed on a cut-away perspective of the NP topography. The magnitude of the field is normalized to the maximum electric field inside the NP. c) A heat-map of the magnitude of the electric field for a 5-NP chain is shown superimposed on a cross-section through the same core-shell NP. The magnitude of the field is normalized to the maximum electric field in the entire computational area.

low loss of (off-resonant) dielectrics causes the Mie resonances of PMs to be narrow, making it difficult to overlap two sets of resonances without precise control of the diameter and position otherwise.

By integrating the complexity of a core-shell structure into a NP, it may be possible to relieve some of the difficulties encountered in the assembly of a PM consisting of different, but homogeneous NPs of different sizes or shapes. In particular, using permittivity recovery techniques and then incorporating those results into an effective medium model,<sup>[288]</sup> it can be shown that three core-shell NPs with realistic material parameters, (i.e. a  $\text{SiO}_2$  core with a 30 nm diameter and Au-shell that is 20 nm thick, **Figure 10a**), exhibit a minimum in  $\text{Re}(\epsilon) = -3$  near  $\lambda = 700$  nm and a broad ENZ band that could be leveraged to create extraordinary optical components such as reflection-less waveguide bends and corners.<sup>[289]</sup> Interestingly, with an increasing chain length, the spectral region of negative permittivity red-shifts. Further analysis has revealed that the electric field for chains of core-shell NPs depends on several factors, including the NP spacing and the location of the NP in the chain (Figure 10b,c). Specifically, when illuminated with a plane wave, the NP no longer appears as a simple dipole to the incident field. This design shows that core-shell NPs stacked together could be used to manufacture ENZ metamaterials.

#### 4.4. PM Assembly via Modular Construction Using Light Gradients

Optical trapping has been used to assemble microscopic particles (e.g. 1  $\mu\text{m}$  diameter microspheres) in 1D,<sup>[112,290]</sup> 2D,<sup>[98,291–297]</sup> or 3D<sup>[298–300]</sup> arrays, but not NPs generally. A 1D array can be created using a SWOT; the antinodes in a standing wave generated by two counter-propagating Gaussian beams trap particles

in an array. For example, Stewart *et al.*<sup>[290]</sup> used optical tweezers this way to assemble into a nanowire-like super-structure superstructure of commercially available, bright, fluorescent nanodiamonds. 2D and 3D PMs can be created from arrays of traps using holographic optical tweezers (HOT). A HOT diffractive element partitions a single collimated laser beam into several beamlets each of which can be focused into the back aperture of an objective lens with a slightly different incident angle, and then re-focused to create an array of traps.<sup>[97]</sup> Recently, a computer-controlled, liquid crystal spatial light modulator (SLM) was used to create HOTs that can be dynamically reconfigured into a variety of patterns.<sup>[292]</sup> For example, Curtis, *et al.*<sup>[98]</sup> demonstrated that HOTs formed with an SLM can be used to create a 2D square lattice as well as circular and other randomly shaped arrays.<sup>[293,294]</sup> However, Lee *et al.*<sup>[301]</sup> write that accurate control of HOTs is limited by the inferior axial resolution that is due to the limited numerical aperture of the imaging system, which physically restricts the information in the vertical direction. As a quick fix, an SLM can be implemented using wave-front modulation methods, such as polarization multiplexing<sup>[302]</sup> and division of an SLM face.<sup>[303]</sup> Other practical problems for using HOTs for trapping are the limited number of pixels, the optical damage threshold, and the sluggish refresh rate.<sup>[302,303]</sup> A nematic liquid-crystal SLM, one of the most widely used types, typically exhibits a low damage threshold ( $<100 \text{ W cm}^{-2}$ ), a zero-order diffraction efficiency of only 61%, an rms wavefront distortion of  $\lambda/5$  (@785 nm) and a slow switching rate (58 Hz @ 785 nm).

#### 4.5. Time-Shared Optical Traps

Whereas a HOT focuses multiple beams simultaneously in a plane to create an array of optical traps, a 2D array can also be created by time-sharing (or time-multiplexing) a single, focused laser beam across a pattern.<sup>[99]</sup> The main idea is that the beam rapidly scans from site-to-site, lingering fleetingly at a position for a time,  $\tau_{\text{light}}$ , just long enough to illuminate a particle and trap it there. In the meantime, when the particle is in the dark for a time,  $\tau_{\text{dark}}$ , it diffuses out of position and so, timing is very important. Typically, the NP position is illuminated or the trap is refreshed at  $\approx$  a 5–10 Hz rate with a duty cycle that depends on the ratio  $\tau_{\text{light}}/\tau_{\text{dark}}$ . This can be accomplished using diffractive elements such as an acousto-optic deflector (AOD) or an electro-optic deflector (EOD) or an SLM (Figure 7a-c).

In response to a radio frequency (RF) signal, an AOD produces ultrasonic acoustic waves that travel across a transparent crystal practically orthogonal to the laser beam.<sup>[304]</sup> The ultrasonic wave generates a diffraction grating with an efficiency that scales with the RF amplitude driving it. The laser diffracts from this grating with an irradiance of  $\approx 60\%$  typically. In principle, the AODs specifications are well suited to time-sharing an optical trap due to the fast response time ( $<10 \mu\text{s}$ ), but in practice it's limited by the ratio of the laser beam diameter to the speed of sound in the crystal and a moderate deflection angle (30 mrad or  $\approx 2^\circ$ ). So, AODs offer dynamic control over the beam position allowing for the creation and manipulation of heterogeneous arrays<sup>[10]</sup> easily<sup>[292,298]</sup>—several array geometries have been created this way such as circular, square, triangular and hexagonal, Penrose quasi-crystals, and even in a random-shaped array with

sub-wavelength spacing (625 nm) between NPs. However, AODs can introduce distortions in the laser beam due to systematic angular deviations from a linear response to the acoustic drive frequency—that result in 10–20 nm variations in the trap position, which have been attributed to partial reflections that result in standing acoustic waves.<sup>[304]</sup>

Alternatively, Woody *et al.*,<sup>[304]</sup> Visscher *et al.*<sup>[291]</sup> and Valentine *et al.*<sup>[292]</sup> report that EODs have advantages over AODs for high resolution optical trapping. Following Visscher, an EOD deflects light using the refractive index gradient created by voltage applied across an electro-optic material. The optical throughput can be as high as 90% and the switching time is relatively fast (100 ns) compared to an AOD. However, like an AOD, an EOD also distorts wave fronts and the maximum deflection angle is <2 mrad, which resulted in a 1 μm separation between traps in their implementation.

Assembling 3D structures using optical trapping can be accomplished one particle at a time using a computer controlled automated system<sup>[127]</sup> or by stacking layers of 2D arrays,<sup>[126,305–309]</sup> but these processes are laborious and time-consuming. The process typically takes place inside a microfluidic chamber having two distinct compartments<sup>[308]</sup> defined as acquisition and assembly areas. In the acquisition area, a 2D array is created using either a HOT or time-shared optical trap and then it is transferred to the assembly area where micro-particle layers are stacked one-by-one to create a 3D structure. According to Melzer's report,<sup>[126]</sup> the particles were subsequently fixed in position either by using avidin and biotin-coated functionalized micro-particles on a biotin-coated microscope slide, or by building the structure in photo-curable pre-polymer medium. Depending on the biotin-PEG-silane concentration, arrays of (1 μm diameter) micro-particles have been assembled this way with a positional accuracy of 60–70 nm.<sup>[126]</sup> Since each particle can be placed in the array one-at-a-time, almost any heterogeneous structure could be assembled this way, but the throughput is abysmal and doesn't scale economically for manufacturing.

To improve the throughput, one avenue utilizes a rapidly scanned, single-beam, gradient force trap to create multiple optical traps for manipulating NPs within a volume (as large as 8000 μm<sup>3</sup>) by time-sharing. Molloy<sup>[92]</sup> and others<sup>[10,97,298–301,309]</sup> have deduced several conditions for trapping according to a time-sharing strategy. From these conditions an estimate of the number of traps that such a strategy can support can be estimated. To be concrete, let's consider the prospects for producing a stable array of a number of silica NPs,  $N$ , with radius  $a = 50$  nm using a time-shared, single-beam, optical trap with a waist  $w_0 = 228$  nm.

1) If the trap location is temporarily in the dark, the NP may diffuse out of the capture range for that trap. For a spherical NP, the diffusion coefficient is  $D = k_B T / 6\pi\eta a$ , where  $\eta$  is the viscosity of the medium,  $k_B$  is Boltzmann's constant and  $T$  is the absolute temperature. If the medium is water at room temperature, then  $\eta = 1.025 \times 10^{-3}$  N·s m<sup>-2</sup>. For a 50 nm spherical NP in water, it is estimated that  $D = 4.4 \times 10^{-12}$  m<sup>2</sup>s<sup>-1</sup>. Correspondingly, the mean square motion is given by the product of the diffusion coefficient and the dark time  $\langle x^2 \rangle \approx (4 \times 0.280 \mu\text{m})^2 = 2 D \tau_{\text{dark}}$ . Consequently, the maximum dark time would be about  $\tau_{\text{dark}} = 6\pi\eta a (2w_0)^2 / 2k_B T < 40$  ms.

2) The time required to restore a 50 nm radius NP to its proper position in the trap will depend on the stiffness of the optical trap  $\kappa < 0.5$  pN/nm. By balancing the optical force against the product of the viscous drag coefficient for a spherical NP and the velocity, we find that:  $F = 6\pi\eta a v = \kappa x$ , where  $v$  is the velocity of the liquid, so that  $\tau_{\text{light}} = x/v = 6\pi\eta a / \kappa = 2$  μs. So, the minimum time required for restoring the particle to its position is about  $\tau_{\text{light}} > 2$  μs.

Based on these estimates, a prescription develops for the duty cycle and the number of NPs that can be effectively trapped by scanning a single-beam:

$$N = \frac{\tau_{\text{dark}}}{\tau_{\text{light}}} = \frac{6\pi\eta a \cdot (2w_0)^2 / 2k_B T}{6\pi\eta a / \kappa} = \frac{2w_0^2 \kappa}{k_B T} \\ = \frac{64P}{3k_B T \cdot w_0^2 c} a^3 (n_p - n_m) \approx 2 \times 10^4 \quad (9)$$

This estimate represents an upper bound on the number and shows how it depends on the laser power, the beam waist, the index difference between the particle and the beam, and sensitively on the size of the particle. It indicates that a SWOT with  $P = 1.5$  W,  $\kappa < 1$  pN nm<sup>-1</sup>) and a beam waist  $w_0 = 228$  nm can be used to trap  $\approx 10^4$  NPs with radius  $a = 50$  nm. According to this expression, the irradiance required to stabilize a NP with a small radius grows geometrically (like  $a^3$ ), however. It is limited in practice by the optical coatings and absorption/reflection from the optics, generally, which inevitably affects the transmitted wave front.

Mindful of these limitations, to facilitate assembly, NPs are conveyed in fluid using multiple laminar flows in a multi-port microfluidic device within the field of view of an array of time-shared, standing wave optical traps formed over a “hot” mirror (Figure 7, center). The convective flow of the fluid used to convey NPs within the field of view for trapping exerts a viscous drag on the NPs, which must not exceed the light gradient force for a stable trap. The magnitude of that force from Stokes law is:  $F = 6\pi\eta a v$ . For a NP with  $a = 50$  nm radius in a flow of water ( $\eta_w = 1.025 \times 10^{-3}$  N·s m<sup>-2</sup>) with a velocity of 1000 μm s<sup>-1</sup>, the particle experiences a force of only  $F \sim 2pN$ , which is much smaller than the gradient force (<100 pN). However, the force increases if the viscosity increases: e.g. for glycerin ( $\eta_{\text{glycerin}} = 1.5$  N·s m<sup>-2</sup>) so that the force required can become comparable to the light gradient force.

Generally, multiple time-multiplexed traps can be generated in 2D or 3D by using a combination of AODs, with or without an SLM and/or a “hot” mirror. Briefly, the diffractive optical elements, the AODs and SLM, are placed in planes conjugate to the back aperture of the microscope objective using relay lenses. The laser is deflected transverse to the direction of propagation using the two orthogonally mounted AODs, giving independent control of the  $x$ - and  $y$ -positions of a trap and allowing for the creation of a 2D network of time-shared traps. Alternatively, the SLM can be used as a Fresnel lens to offset the array along the optical axis or alone to generate a hologram, where multiple optical traps are created simultaneously by controlling the intensity and phase profile of the beam.

Using a tool configured this way (Figure 7), it is possible to combine different sizes of dielectric NPs either by incorporating

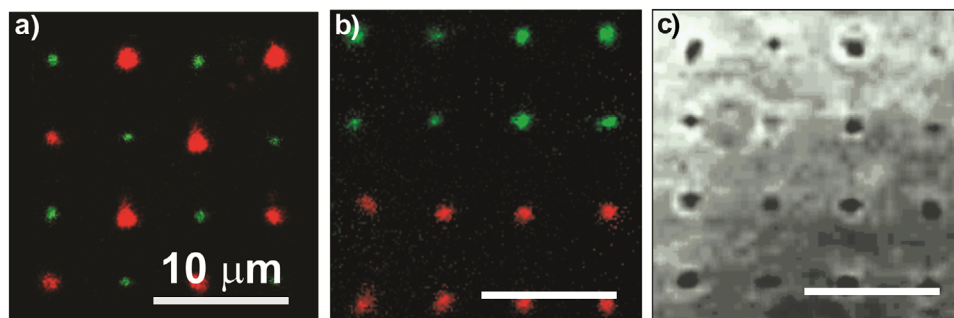


**Figure 11.** 2D heterogeneous arrays assembled differently with light gradients. a) A confocal fluorescence image taken from a regular lattice consisting of four  $2 \times 2$  heterogeneous voxels is shown assembled using a time-multiplexed Gaussian beam in combination with a “step-and-repeat” method. Each voxel consists of two types of fluorescent polystyrene NPs with nominally 350- (green) and 1000 nm (red) diameters. The separation between NPs was  $5,570 \pm 35$  nm. b) Like (a), but the heterogeneous lattice was formed from homogeneous voxels consisting of either nominally 200- (red) or 350-nm- (green) diameter fluorescent polystyrene NPs. The separation between NPs was  $6090 \pm 250$  nm. c) A single heterogeneous  $4 \times 4$  voxel consisting of alternating columns of 350-nm-diameter fluorescent polystyrene and silica NPs is shown. A time-multiplexed Gaussian beam with an irradiance of  $P = 200$  mW at  $\lambda_0 = 866$  nm was used to create each voxel. Adapted from ref. [10].

them into the same voxel or by using a combination of a Gaussian beam and a “step-and-repeat” method to place them on the same lattice (Figure 11). Whereas optical trapping allows for the creation of complex heterogeneous arrays of NPs, the light still has to be held on them to maintain the array. So, to temporarily fix the position of the NPs without light, a scaffold made from a photo-polymerizable hydrogel was used.<sup>[10,299,300]</sup> Subsequently, each voxel is then stitched together with the last to create a super-array of any size, shape and constituency using a “step-and-repeat” strategy like that used for lithography in semiconductor manufacturing to print a die. For illustration, the heterogeneous 2D super-lattice of NPs shown in Figure 11a was assembled from fluorescent NPs; each voxel consisted of two types of fluorescent polystyrene NPs with nominally 350- (green) and 1000 nm (red) diameters. On the other hand, the heterogeneous lattice shown in Figure 11b was formed from homogeneous voxels consisting of either nominally 200- (red) or 350-nm- (green) diameter fluorescent polystyrene NPs. Different materials can be assembled on the same lattice as well, as illustrated for 350 nm diameter silica and polystyrene NPs in Figure 11c. A further illustration of how the tool can be used, examples of dielectric “voxels” created this way are shown in Figure 7a–c. The array shown in Figure 7a is a single voxel consisting of a 3D super-lattice of  $1 \times 3$  arrays consisting of 500 nm-diameter dielectric NPs formed using an SLM; Figure 7b shows a 2D– $16 \times 16$  array of 200 nm dielectric NPs assembled using a time-shared optical tweezers; and Figure 7c is a 2D– $4 \times 4$  array of 500 nm-diameter  $\text{SiO}_2@Au$  core-shell NPs also assembled using a time-shared optical tweezers. (In the latter implementations the SLM was replaced by a mirror.)

Coherent scattering from an ensemble of NPs informs on the entire lattice structure “defects and all” through the interference between the scattered waves. Lattice imperfections and registration errors introduce phase noise that could adversely affect the interference. To expose the defects and discover their origin, a  $4 \times 4$  lattice of  $2 \times 2$  voxels, spaced  $\approx 10,000$  nm apart, comprising an  $8 \times 8$  super-lattice assembled from (nominally) 100 nm radius NPs using a time-multiplexed 70 mW GSWOT at  $\lambda_0 = 862$  nm was analyzed (Figure 12a). After iterative de-convolution of the confocal fluorescence image shown in Figure 12a, an

estimate for the NP radius, compiled from ( $x$ -,  $y$ -) measurements across the entire lattice, revealed a radius of  $105 \pm 5$  nm, which was consistent with the nominal radius within the 3% CV (Figure 12b). It was observed that the NPs were stacked eight-to-ten deep along the  $z$ -axis with successive fluorescence intensity maxima (Figures 12b,c) spaced  $\Delta z = 294$  nm, which was smaller, but in line with the distance between anti-nodes in the standing wave,  $\Delta z_+ = \lambda/2n_m = 324$  nm (Figure 12d). Measurements of the intra-voxel lattice constant (within each voxel) averaged over the entire super-lattice of voxels were  $\delta X = 4937$  nm and  $\delta Y = 5087$  nm with a minimum (Gaussian) standard deviation of  $\sigma_{Xmin} = 51$  nm along  $x$  and  $\sigma_{Ymin} = 89$  nm along  $y$ , whereas the inter-voxel lattice constants were  $\delta X = 4737$  nm and  $\delta Y = 5022$  nm with slightly larger minimum standard deviations of  $\sigma_{Xmin} = 71$  nm and  $\sigma_{Ymin} = 93$  nm. The placement error was conspicuous when the voxels were superimposed (Figure 12e). It was evident that the placement error within a voxel was related mainly to Brownian motion in a dark trap, which coincidentally was about the distance (35 nm) a 100 nm-radius particle diffuses when the lattice position was in the dark,<sup>[10]</sup> but the repeatability of the position of the microscope stage and the hydrogel photo-polymerization of neighboring voxels were also implicated in the misalignment between voxels.

The cross-linked PEGDA scaffold was too compliant to be practical. According to nano-indentation the Young’s modulus is only  $\approx 200$  kPa with a mesh size,  $\zeta < 4$  nm.<sup>[310]</sup> The stiffness can be improved to  $\approx 1$  GPa when the concentration of PEGDA is increased 60% (w/v) in the pre-polymer mix, but the viscosity deteriorates so much so that a NP cannot be easily manipulated by hand. Since the PEGDA hydrogel is permeable to small molecules,<sup>[310,311]</sup> to produce more robust PMs, the scaffold was vitrified with tetraethyl orthosilicate (TEOS) following Bohn *et al.* without disrupting the array.<sup>[10]</sup> TEOS degrades in water or high temperature to form glass,  $\text{SiO}_2$ . So, after assembly, to vitrify the metamaterial, first it is flushed with ethanol to remove the PEGDA precursor and water, and then TEOS (in ethanol and water) is injected into the microfluidic device to infiltrate through the scaffold. Relying on well-established sol-gel chemistry that has been used in the synthesis of  $\text{SiO}_2$  xerogels, NPs, and coatings, the TEOS subsequently converted to  $\text{SiO}_2$  using an acid or

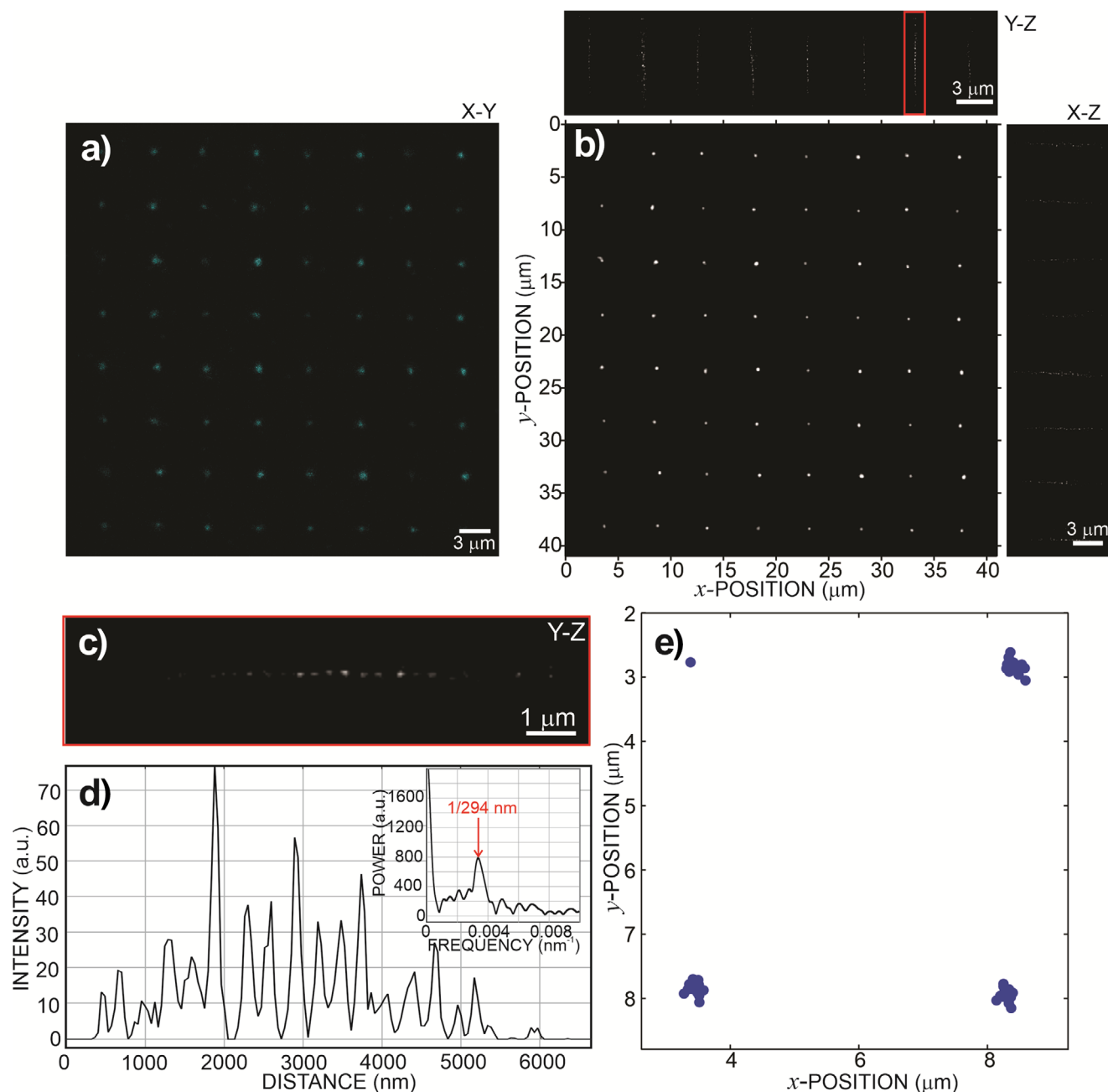


**Figure 12.** Modular assembly of macroscopic 3D NP lattice using light gradients. a) An optical micrograph is shown of an X-Y view acquired from a  $4 \times 4$  super-lattice formed from voxels consisting of  $2 \times 2 (X > 15)$  (nominally) 100 nm-radius fluorescent polystyrene NPs, assembled with a focused time-shared GSWOT in combination with a “step-and-repeat” method. b) A reconstruction of an optical micrograph after deconvolution is shown that was acquired from the super-lattice in (a) illustrating the X-Y, Y-Z, and X-Z structure. c) A Y-Z-view is shown of a typical element highlighted in a red box in the 3D voxel of (b). d) A line-cut through the de-convolved image through the xz-view in (b) is shown illustrating the NP size and the periodicity along the optical axis. (d, inset) The Fourier transform of the X-Y-cross-section in (c) is shown. The power spectrum peaks at a distance between successive fluorescence maxima near  $1/(294 \text{ nm})$ . e) The positional errors within each voxel are shown superimposed on the reference NP (upper left) for the entire  $8 \times 8$  super-lattice along the X-Y-direction. Adapted from ref. [10].

base catalysis. Importantly, a variation of the above method for hydrogel vitrification was recently used to prepare inverse opal crystals for photonic applications.<sup>[312]</sup>

Thus, arrays of any size, shape and constituency can be assembled in 2D or 3D with light gradients using a “step-and-

repeat” methodology in a way akin to modular construction, but the lattices may be imperfect. The prospects for using light gradients for the assembly of PMs from dielectric NPs this way were subsequently tested and the NIR performance was analyzed with angle-, wavelength-, and polarization-dependent reflection

**Table 1.** A summary of the various methods used in the fabrication of metamaterials.

Method	Minimum Feature Size	Advantages	Disadvantages
NIL (Nanoimprint Lithography)	> 10 nm	<ul style="list-style-type: none"> <li>high throughput;</li> <li>relatively low cost (compared to EBL);</li> <li>large area patterning.</li> </ul>	<ul style="list-style-type: none"> <li>mold fabrication expensive with limited resolution;</li> <li>molds can be defective with contact,</li> <li>overlay accuracy problematic.</li> </ul>
EBL (Electron Beam Lithography)	< 10 nm	<ul style="list-style-type: none"> <li>high resolution;</li> <li>direct-write (no mask);</li> <li>flexibility in pattern design.</li> </ul>	<ul style="list-style-type: none"> <li>(serial) low throughput → high cost,</li> <li>proximity effects distort patterns;</li> <li>conductive substrates;</li> <li>registration errors over large areas</li> </ul>
RIE (Reactive Ion Etching)	< 1 nm	<ul style="list-style-type: none"> <li>anisotropic (vertical sidewalls);</li> <li>selectivity;</li> <li>crucial for pattern transfer.</li> </ul>	<ul style="list-style-type: none"> <li>process optimization complex;</li> <li>surface damage;</li> <li>loading → non-uniform etch</li> </ul>
ALD (Atomic Layer Deposition)	< 1 nm	<ul style="list-style-type: none"> <li>conformal;</li> <li>tight thickness control;</li> <li>pinhole-free.</li> </ul>	<ul style="list-style-type: none"> <li>slow deposition rate;</li> <li>limited materials selection;</li> <li>expensive for large-scale production</li> </ul>
CVD (Chemical Vapor Deposition)	> 10 nm	<ul style="list-style-type: none"> <li>high deposition rate;</li> <li>wide range of materials;</li> <li>conformal coating.</li> </ul>	<ul style="list-style-type: none"> <li>requires high temperature;</li> <li>toxic precursors;</li> <li>non-uniformity over large areas;</li> <li>lacks atomic-level control like ALD.</li> </ul>
MPP (Multiphoton Polymerization)	> 100 nm	<ul style="list-style-type: none"> <li>3D fabrication of complex structures.</li> </ul>	<ul style="list-style-type: none"> <li>(serial) low throughput;</li> <li>limited materials selection.</li> </ul>
Block Copolymer Self-Assembly	> 10 nm	<ul style="list-style-type: none"> <li>High-throughput;</li> <li>periodic nanostructures over large areas.</li> </ul>	<ul style="list-style-type: none"> <li>limited pattern complexity;</li> <li>defect control problematic;</li> <li>demands specific material combos;</li> <li>pattern transfer to functional materials unavailable.</li> </ul>
Colloidal Crystal Self-Assembly	> 100 nm	<ul style="list-style-type: none"> <li>scalable for periodic structures;</li> <li>can create photonic crystals + templates for metamaterials.</li> </ul>	<ul style="list-style-type: none"> <li>Limited pattern complexity beyond periodic arrays;</li> <li>defect control problematic;</li> <li>demands precise control over colloidal interactions.</li> </ul>
Martensitic Phase Transformations	atomistic	<ul style="list-style-type: none"> <li>complex microstructures with specific mechanical and functional properties can be created;</li> <li>self-actuating capabilities.</li> </ul>	<ul style="list-style-type: none"> <li>limited materials;</li> <li>precise control over domain size/orientation problematic;</li> <li>specific thermal cycling protocols required.</li> </ul>
Modular Assembly with Light Gradients	> 10 nm	<ul style="list-style-type: none"> <li>contactless and dynamic assembly of micro/nanoparticles into complex structures;</li> <li>wide range of materials.</li> </ul>	<ul style="list-style-type: none"> <li>scalable to large-area fabrication (step-and-repeat);</li> <li>demands precise control of laser beam;</li> <li>stringent control of particle size/index.</li> </ul>

spectroscopy.<sup>[10]</sup> Due to the unusually strong polarization sensitivity of electric and magnetic dipole resonances, Mie resonance scattering peculiar to the NP size was exposed this way.<sup>[10]</sup> Both Bragg and Mie scattering have been observed in collections of (spherical) NPs before.<sup>[58,314]</sup> However, disorder that introduces random phase-shifts and amplitude variations can have an adverse effect on the band structure producing a broad background continuum.

## 5. Summary

In conclusion, the applications for metamaterials are legion, but their promise can't be exploited in earnest and the market for them cannot grow unless a facile and economical method for fabricating them free of defects emerges. Commercial computational tools like COMSOL are available for the rational design of PMs. Leveraging tools like this for simulations, designs for metamaterials and meta-surfaces have been implemented with "Homeric" effort using "top-down" and "bottom-up" methods to assess the optical performance. These methods have been explored exhaustively and have laid bare some of the limita-

tions that frustrate manufacturing (see **Table 1**). Among the limitations are: the wide assortment of materials, which include metals like *Au*, *Ag*, *Ni(P)*, *TiN*; dielectrics like indium-tin-oxide (ITO), *ZnO(Al)*, *Si*, silica, rutile, and *C*(diamond); perovskite like *SrSnO<sub>3</sub>*; plastics like latex, polypropylene (PP), polylactic acid (PLA), pentaerythritol triacrylate (PETA) and ceramics made from pyrolytic carbon; imperfections (unintentional defects) in the construction especially at the nanometer-scale due to lithography or etch; and the absence of batch processing or even wafer-scale processing (with few exceptions) for high volume manufacture. For example, while it is possible to draw structures with sub-micron resolution using direct (laser) writing or additive manufacturing techniques, they are slow, serial processes limited by the speed and precision of the stage, and they're restricted to relatively few materials right now. On the other hand, standard photolithography, with a minimum feature size > 1 μm (the limit of the mask aligner) has produced "hyperlenses" for sub-diffraction imaging on a (3") wafer-scale. EUV photo-lithography combined with "step-and-repeat" offers improved resolution, but it comes at a high cost for the tool and the masks. And finally, NIL can replicate a pattern embedded in a mold with 10 nm resolution

with high productivity, but the stamp is costly and it wears—any defect in it is eventually transferred to the nanostructure.

It's argued here that unintentional defects are at the core of the issues associated with manufacturing. This is apparent in manufacture of ICs and the synthesis of protein. PMs will likely suffer similarly. To become economically viable, this problem has to be resolved.

### 5.1. So What's Next?

To light up metamaterials, we argue for “something completely different”. It is now feasible to manufacture precisely with high yield monodispersed NPs with built-in complexity and assemble them into a metamaterial using a time-shared laser beam.<sup>[10]</sup> The registration is limited by Brownian motion and the precision of the stage. The speed limit is set by the depth of the optical trap, the diffractive elements used to deflect the laser beam and the speed of the stage. Moreover, the 1D array of NPs produced by a Bessel beam SWOT is defective—it has shown vacancies and multiple NPs at a single anti-node. Despite the flaws, it seems feasible to create metamaterials of any size, shape and constituency this way using light gradient forces to assemble NPs.

### Acknowledgements

This work was supported by a Grant AFRL/DARPA FA8650-15-C-7546 from the DARPA A2P2 program and partially supported by the Keough-Hesburgh Professorship. The authors would also like to thank Alexander Volk, Drs. Mohammad Hokmabadi, Eveline Rigo, Ryan K. Roeder, K. Sarveswaran, Profs. Uktur Mirsaidov and A. Hoffman for sharing their expertise and data.

### Conflict of Interest

The authors declare no conflict of interest.

### Keywords

metamaterials, meta-surfaces, optical tweezers, optical trapping

Received: February 14, 2025  
Revised: April 30, 2025  
Published online:

- [1] U. Zywiets, A. B. Evlyukhin, C. Reinhardt, B. N. Chichkov, *Nat. Commun.* **2014**, *5*, 3402.
- [2] M. Kadic, T. Bückmann, N. Stenger, M. T. N., M. Wegener, *Appl. Phys. Lett.* **2012**, *100*, 191901.
- [3] A. Prakash, T. Wang, A. Bucsek, T. K. Truttmann, A. Fali, M. Cotrufo, H. Yun, J.-W. Kim, P. J. Ryan, K. A. Mkhoyan, A. Alù, Y. Abate, R. D. James, B. Jalan, *Nano Lett.* **2021**, *21*, 1246.
- [4] D. Lin, P. Fan, E. Hasman, M. L. Brongersma, *Science* **2014**, *345*, 298.
- [5] M. Thiel, M. S. Rill, G. Von Freymann, M. Wegener, *Adv. Mater.* **2009**, *21*, 4680.
- [6] a) J. Kaschke, M. Wegener, *Opt. Lett.* **2015**, *40*, 3986s; b) J. K. Gansel, M. Thiel, M. S. Rill, M. Decker, K. Bade, V. Saile, G. von Freymann, S. Linden, M. Wegener, *Science* **2009**, *325*, 1513.
- [7] J. Zhou, I. Dong, B. Wang, T. Koschny, M. Kafesaki, C. M. Soukoulis, *Phys. Rev. B* **2009**, *79*, 121104(R).
- [8] J. Valentine, S. Zhang, T. Zentgraf, E. Ulin-Avila, D. A. Genov, G. Bartal, X. Zhang, *Nature* **2008**, *455*, 376.
- [9] D. B. Burckel, J. R. Wendt, G. A. T. Eyck, J. C. Ginn, A. R. Ellis, I. Brener, M. B. Sinclair, *Adv. Mater.* **2010**, *22*, 5053.
- [10] A. Paul, A. Volk, M. Hokmabadi, E. Rigo, H. Kermani, L. Almonte-Garcia, T. A. Finamore, K. M. Iwamoto, R. K. Roeder, G. Timp, *Adv. Mater.* **2024**, *36*, 2401344.
- [11] I. Staude, A. E. Miroshnichenko, M. Decker, N. T. Fofang, S. Liu, E. Gonzales, J. Dominguez, T. S. Luk, D. N. Neshev, I. Brener, Y. Kivshar, *ACS Nano* **2013**, *7*, 7824.
- [12] J. Yao, Z. Liu, Y. Liu, Y. Wang, C. Sun, G. Bartal, X. Z. A. M. Stacy, *Science* **2008**, *321*, 930.
- [13] M. Decker, M. Ruther, C. E. Krieglger, J. Zhou, C. M. Soukoulis, S. Linden, M. Wegener, *Opt. Lett.* **2009**, *34*, 2501.
- [14] X. Zheng, W. Smith, J. Jackson, B. Moran, H. Cui, D. Chen, J. Ye, N. Fang, N. Rodriguez, T. Weisgraber, C. M. Spadaccini, *Nat. Mater.* **2016**, *15*, 1100.
- [15] S. Wong, M. Deubel, F. Pérez-Willard, S. John, G. A. Ozin, M. Wegener, G. Von Freymann, *Adv. Mater.* **2006**, *18*, 265.
- [16] J. Bauer, A. Schroer, R. Schwaiger, O. Kraft, *Nat. Mater.* **2016**, *15*, 438.
- [17] B. J. Hunt, *The Maxwellians*, Cornell University Press, Ithaca, New York **1991**.
- [18] J. C. Bose, *Proc. Royal Soc. London* **1898**, *63*, 389.
- [19] V. G. Veselago, *Sov. Phys. Usp.* **1968**, *10*, 509.
- [20] J. B. Pendry, A. J. Holden, W. J. Stewart, I. Youngs, *Phys. Rev. Lett.* **1996**, *76*, 4773.
- [21] J. B. Pendry, A. J. Holden, D. J. Robbins, W. J. Stewart, *J. Phys.: Condens. Matter.* **1998**, *10*, 4785.
- [22] J. B. Pendry, A. J. Holden, D. J. Robbins, W. J. Stewart, *IEEE Trans. Microwave Theory Technol.* **1999**, *47*, 2075.
- [23] <https://www.imarcgroup.com/metamaterials-market> (accessed: May 2025).
- [24] a) D. Patel, A. Ahmad, “TSMC 3nm FinFlex + Self-Aligned Contacts, Intel EMIB 3 + Foveros Direct, AMD Yield Issues, IBM Vertical Transport FET (VTFET) + RU Interconnects, CFET, Sequential Stacking, Samsung Yield, and more //IEDM 2022 Round-Up,” <https://semianalysis.com/2023/02/02/iedm2022p1/> (accessed: February 2023); b) M. S. Bhoir, T. Chiarella, L. A. Ragnarsson, J. Mitard, V. Terzeiva, N. Horiguchi, N. R. Mohapatra, *IEEE J. Electron Devices Soc.* **2019**, *7*, 1217.
- [25] <https://www.macrumors.com/2024/09/19/kuo-iphone-17-3nm-chips/> (accessed: May 2025).
- [26] <https://www.anandtech.com/show/16041/where-are-my-gaafets-tsmc-to-stay-with-finfet-for-3nm> (accessed: May 2025).
- [27] C.-H. Chang, V. S. Chang, K. H. Pan, K. T. Lai, J. H. Lu, J. A. Ng, C. Y. Chen, B. F. Wu, C. J. Lin, C. S. Liang, C. P. Tsao, Y. S. Mor, C. T. Li, T. C. Lin, C. H. Hsieh, P. N. Chen, H. H. Hsu, J. H. Chen, H. F. Chen, J. Y. Yeh, M. C. Chiang, C. Y. Lin, J. J. Liaw, C. H. Wang, S. B. Lee, C. C. Chen, H. J. Lin, R. Chen, K. W. Chen, C. O. Chui, presented at 2022 *Int. Electron Devices Meeting (IEDM)*, San Francisco, CA, USA, December **2022**, <https://doi.org/10.1109/IEDM45625.2022.10019565> (accessed: May 2025).
- [28] X. Guo, Z. Xue, Y. Zhang, *NPG Asia Mater.* **2019**, *11*, 29.
- [29] Y. Akasaka, *Proc. IEEE* **1986**, *74*, 1703.
- [30] W. R. Davis, J. Wilson, S. Mick, J. Xu, H. Hua, C. Mineo, A. M. Sule, M. Steer, P. D. Franzon, *IEEE Design Test Comput.* **2005**, *22*, 498.
- [31] K. Bernstein, R. Puri, A. Young, P. Andry, J. Cann, P. Emma, D. Greenberg, W. Haensch, M. Ignatowski, S. Koester, J. Magerlein, in *Proc. of the 44th Annual Conf. on Design Automation – DAC '07*, ACM Press, San Diego, California, **2007**, p. 562–567.
- [32] P. R. Morrow, C.-M. Park, S. Ramanathan, M. J. Kobrinsky, M. Harmes, *IEEE Electron Device Lett.* **2006**, *27*, 335.

- [33] <https://www.tomshardware.com/tech-industry/tsmcs-wafer-pricing-now-usd18-000-for-a-3nm-wafer-increased-by-over-3x-in-10-years-analyst> (accessed: May 2025).
- [34] <https://www.construction-physics.com/p/how-to-build-a-20-billion-semiconductor> (accessed: May 2024).
- [35] M. Horiguchi, J. Etoh, M. Aloki, K. Itoh, T. Matsumoto, *IEEE J. Solid-State Circ.* **1991**, 26, 12.
- [36] <https://www.trendforce.com/news/2024/09/12/news-samsungs-2nm-yield-rate-at-most-20-withdraws-personnel-from-texas-taylor-plant/> (accessed: May 2025).
- [37] <https://www.statista.com/outlook/tmo/semiconductors/integrated-circuits/worldwide> (accessed: May 2025).
- [38] J. Jumper, R. Evans, A. Pritzel, T. Green, M. Figurnov, O. Ronneberger, K. Tunyasuvunakool, R. Bates, A. Žídek, A. Potapenko, A. Bridgland, C. Meyer, S. A. A. Kohl, A. J. Ballard, A. Cowie, B. Romera-Paredes, S. Nikolov, R. Jain, J. Adler, T. Back, S. Petersen, D. Reiman, E. Clancy, M. Zielinski, M. Steinegger, M. Pacholska, T. Berghammer, S. Bodenstein, D. Silver, O. Vinyals, et al., *Nature* **2021**, 577, 583.
- [39] G. Ahdriz, N. Bouatta, C. Floristean, S. Kadyan, Q. Xia, W. Gerecke, T. J. O'Donnell, D. Berenberg, I. Fisk, N. Zanichelli, B. Zhang, A. Nowaczynski, B. Wan, M. M. Stepniewska-Dziubinska, S. Zhang, A. Ojewole, M. E. Guney, S. Biderman, A. M. Watkins, S. Ra, P. R. Lorenzo, L. Nivon, B. Weitzner, Y.-E. A. Ban, S. Chen, M. Zhang, C. Li, S. L. Song, Y. He, P. K. Sorger, et al., *Nat. Methods* **2024**, 21, 1514.
- [40] K. Swanson, G. Liu, D. B. Catacutan, A. Arnold, J. Zou, J. M. Stokes, *Nat. Mach. Intel.* **2024**, 6, 338.
- [41] <https://magazine.hms.harvard.edu/articles/did-ai-solve-protein-folding-problem> (accessed: May 2025).
- [42] G. M. Whitesides, B. Grzybowski, *Science* **2002**, 295, 2418.
- [43] A. van Blaaderen, R. Ruel, P. Wiltzius, *Nature* **1997**, 385, 321.
- [44] M. M. Burns, J. M. Fournier, J. A. Golvchenko, *Science* **1991**, 249, 749.
- [45] J. Y. Cheng, C. A. Ross, E. L. Thomas, H. I. Smith, G. J. Vansco, *Appl. Phys. Lett.* **2002**, 81, 3657.
- [46] T. Thurn-Albrecht, *Science* **2000**, 290, 2126.
- [47] J. Bodycomb, Y. Funaki, K. Kimishima, T. Hashimoto, *Macromolecules* **1999**, 32, 2075.
- [48] C. J. Guerrero, J. L. Brodsky, *Physiol. Rev.* **2012**, 92, 537.
- [49] T. K. Chaudhuri, S. Paul, *FEBS J.* **2006**, 273, 1331.
- [50] U. Schubert U, L. C. Anton, J. Gibbs, C. C. Norbury, J. W. Yewdell, J. R. Bennink, *Nature* **2000**, 404, 770.
- [51] O. J. Wouters, M. McKee, J. Luyten, *J.A.M.A.* **2020**, 323, 844.
- [52] <https://amr.solutions/2020/03/06/what-does-an-antibiotic-cost-to-develop-what-is-it-worth-how-to-afford-it/> (accessed: May 2025).
- [53] Z.-Y. Li, Z.-Q. Zhang, *Phys. Rev. B* **2000**, 62, 1516.
- [54] R. E. Jorgenson, L. I. Basilio, W. A. Johnson, L. K. Warne, D. W. Peters, D. R. Wilton, R. Capolino, *Sandia Rep.* **2006**, 6833.
- [55] S. C. L. Fischer, L. Hillen, C. Eberl, *Materials* **2020**, 13, 3605.
- [56] A. A. Zadpoor, M. J. Mirzaali, L. Valdevt, J. B. Hopkins, *Appl. Phys. Lett. Mater.* **2023**, 11, 020401.
- [57] A. S. Solntsev, G. S. Agarwal, Y. S. Kivshar, *Nat. Photonics* **2021**, 15, 327.
- [58] A. I. Kuznetsov, A. E. Miroshnichenko, M. L. Brongersma, Y. S. Kivshar, B. Luk'yanchuk, *Science* **2016**, 354, 846.
- [59] M. F. Limonov, M. V. Rybin, A. N. Poddubny, Y. S. Kivshar, *Nat. Photonics* **2017**, 11, 543.
- [60] S. Jahani, Z. Jacob, *Nat. Nanotech.* **2016**, 11, 23.
- [61] C. M. Soukoulis, M. Wegener, *Nat. Photonics* **2011**, 5, 523.
- [62] Y. Liu, X. Zhang, *Chem. Soc. Rev.* **2011**, 40, 2494.
- [63] A. Ali, A. Mitra, B. Aïssa, *Nanomaterials* **2022**, 12, 1027.
- [64] M. Kadic, G. W. Milton, M. van Hecke, M. Wegener, *Nature Rev. Phys.* **2019**, 1, 198.
- [65] D. Lee, M. Kim, J. Rho, *Micromachines* **2021**, 12, 1142.
- [66] J. E. Holliman, T. Schaefer, B. P. McCraill, Q. Miller, *Mater. Adv.* **2022**, 3, 8390.
- [67] A. Krushynska, D. Torrent, A. Aragón, R. Ardito, O. Bilal, B. Bonello, F. Bosia, Y. Chen, J. Christensen, A. Colombi, S. Cummer, B. Djafari-Rouhani, F. Fraternali, P. Galich, P. Garcia, J. Groby, S. Guenneau, M. Haberman, M. Hussein, S. Janbaz, N. Jiménez, A. Khelif, V. Laude, M. Mirzaali, P. Packo, A. Palermo, Y. Pennec, R. Picó, M. López, S. Rudykh, et al., *J. Nanophotonics* **2023**, 12, 659.
- [68] A. Cummer, J. Christensen, A. Alu, *Nat. Rev. Mater.* **2016**, 1, 016001.
- [69] J. U. Surjadi, L. Gao, H. Du, X. Li, X. Xiong, N. X. Fang, Y. Lu, *Adv. Eng. Mater.* **2019**, 21, 1800864.
- [70] K. Gangwar, D. Paras, R. P. S. Gangwar, *Adv. Electron. Elec. Eng.* **2014**, 4, 97.
- [71] T. Lee, C. Lee, D. K. Oh, T. Badloe, J. G. Ok, J. Rho, *Sensors* **2020**, 20, 4108.
- [72] M. Askari, D. A. Hutchins, P. J. Thomas, L. Astolfi, R. L. Watson, M. Abdi, M. Ricci, S. Laureti, L. Nie, S. Freear, R. Wildman, C. Tuck, M. Clarke, E. Woods, A. T. Clare, *Addit. Manuf.* **2020**, 36, 101562.
- [73] D. K. Oh, T. Lee, B. Ko, T. Badloe, J. G. Ok, J. Rho, *Front. Optoelectron.* **2021**, 14, 229.
- [74] V.-C. Suy, C. H. Chu, G. Sun, D. P. Tsai, *Opt. Express* **2018**, 26, 13418.
- [75] D. Lee, Y. D. Kim, M. Kim, S. So, H.-J. Choi, J. Mun, D. M. Nguyen, T. Badloe, J. G. Ok, K. Kim, H. Lee, J. Rho, *ACS Photonics* **2018**, 5, 2549.
- [76] B. Leng, Y. Zhang, D. P. Tsai, S. Xiao, *Light: Adv. Manufactur.* **2024**, 5, 117.
- [77] Y. I. Abdulkarim, A. Mohanty, O. P. Acharya, B. Appasani, M. S. Kahn, S. K. Mohapatra, F. F. Muhammadsharif, J. Dong, *Front. Phys.* **2022**, 10, 893791.
- [78] X. Zhao, Z. Sun, L. Zhang, Z. Wang, R. Xie, J. Zhao, R. You, Z. You, *Adv. Dev. Instru.* **2022**, 2022, 9765089.
- [79] S. Mühligh, C. Rockstuhl, V. Yannopapas, T. Bürgi, N. Shalkevich, F. Lederer, *Opt. Express* **2011**, 19, 9607.
- [80] C. Rockstuhl, F. Lederer, C. Etrich, T. Pertsch, T. Scharf, *Phys. Rev. Lett.* **2007**, 99, 017401.
- [81] J. Bang, U. Jeong, D. Y. Ryu, T. P. Russell, C. J. Hawker, *Adv. Mater.* **2009**, 21, 4769.
- [82] S. Frein, J. Boudon, M. Vonlanthen, T. Scharf, J. Barberá, G. Süß-Fink, T. Bürgi, R. Deschenaux, *Helv. Chim. Acta* **2008**, 91, 2321.
- [83] P. W. K. Rothmund, *Nature* **2006**, 440, 297.
- [84] Y. Li, H. Jin, W. Zhou, Z. Wang, Z. Lin, C. A. Mirkin, H. D. Espinosa, *Sci. Adv.* **2023**, 9, adj8103.
- [85] S.-W. Hsu, A. L. Rodarte, M. Som, G. Arya, A. R. Tao, *Chem. Rev.* **2018**, 118, 3100.
- [86] J.-H. Huh, K. Kim, E. Im, J. Lee, Y. D. Cho, S. Lee, *Adv. Mater.* **2020**, 32, 2001806.
- [87] J. Dintinger, S. Mühligh, C. Rockstuhl, T. Scharf, *Opt. Mater. Express* **2012**, 2, 269.
- [88] D. G. Grier, *Nature* **2003**, 424, 810.
- [89] R. F. Service, *Science* **2010**, 327, 138.
- [90] G. Timp, R. E. Behringer, D. Tennant, J. E. Cunningham, M. Prentiss, K. K. Berggren, *Phys. Rev. Lett.* **1992**, 69, 1636.
- [91] J. J. McClelland, M. Prentiss, R. Scholten, E. Palm, R. Celotta, *Science* **1993**, 262, 877.
- [92] U. Drodofsky, J. Stuhler, B. Brezger, T. Schulze, M. Drewsen, T. Pfau, J. Mlynek, *Microelectron. Eng.* **1997**, 35, 285.
- [93] B. Brezger, T. Schulze, P. O. Schmidt, R. Mertens, T. Pfau, J. Mlynek, *Eur. Phys. Lett.* **1999**, 46, 148.
- [94] R. W. McGowan, D. M. Giltner, S. A. Lee, *Opt. Lett.* **1995**, 20, 2535.
- [95] T. Seideman, *J. Chem. Phys.* **1997**, 107, 10420.
- [96] B. S. Zhao, H. S. Chung, K. Cho, S. H. Lee, S. Hwang, J. Yu, Y. H. Ahn, J. Y. Sohn, D. S. Kim, W. K. Kang, D. S. Chung, *Phys. Rev. Lett.* **2000**, 85, 2705.

- [97] E. R. Dufresne, D. G. Grier, *Rev. Sci. Instrum.* **1998**, 69, 1974.
- [98] J. E. Curtis, B. A. Koss, D. G. Grier, *Opt. Commun.* **2002**, 207, 169.
- [99] J. E. Molloy, *Methods Cell Biol.* **1998**, 55, 205.
- [100] A. Ashkin, *Phys. Rev. Lett.* **1970**, 24, 156.
- [101] A. Ashkin, *Biophys. J.* **1992**, 61, 569.
- [102] A. Ashkin, J. M. Dziedzic, J. E. Bjorkholm, S. Chu, *Opt. Lett.* **1986**, 11, 288.
- [103] R. M. Simmons, J. T. Finer, S. Chu, J. A. Spudich, *Biophys. J.* **1996**, 70, 1813.
- [104] M. Jahnel, M. Berhrndt, A. Jannasch, E. Schaffer, S. W. Grill, *Opt. Lett.* **2011**, 36, 1260.
- [105] F. Gittes, C. F. Schmidt, *Opt. Lett.* **1998**, 23, 7.
- [106] T. Tlustý, A. Meller, R. Bar-Ziv, *Phys. Rev. Lett.* **1998**, 81, 1738.
- [107] P. Zemanek, A. Jonas, L. Sramek, M. Liska, *Opt. Commun.* **1998**, 151, 273.
- [108] L. P. Ghislain, N. A. Switz, W. W. Webb, *Rev. Sci. Instrum.* **1994**, 65, 2762.
- [109] A. Rohrbach, E. H. K. Stelzer, *Appl. Opt.* **2002**, 41, 2194.
- [110] P. Ke, M. Gu, *Appl. Opt.* **1999**, 38, 160.
- [111] R. Omori, T. Kobayashi, A. Suzuki, *Optics Lett.* **1997**, 22, 816.
- [112] W. Singer, M. Frick, S. Bernet, M. Ritsch-Marte, *J. Opt. Soc. Am. B* **2003**, 20, 1568.
- [113] V. G. Shvedov, A. S. Desyatnikov, A. V. Rode, Y. V. Izdebskaya, W. Z. Krolikowski, Y. S. Kivshar, *Appl. Phys. A* **2010**, 100, 327.
- [114] M. Michihata, T. Hayashi, Y. Takaya, *Appl. Opt.* **2009**, 48, 6143.
- [115] P. Baret, S. Henderson, *J. Phys.: Condens. Matter.* **2002**, 14, 7757.
- [116] A. Ashkin, *Methods Cell Biol.* **1998**, 55, 1.
- [117] Y. Harada, T. Asakura, *Opt. Commun.* **1996**, 124, 529.
- [118] K. Svododa, S. M. Block, *Opt. Lett.* **1994**, 19, 930.
- [119] A. van der Horst, P. D. J. van Oostrum, A. Moroz, A. van Blaaderen, M. Dogterom, *Appl. Opt.* **2008**, 47, 3196.
- [120] J. Liesener, M. Reicherter, T. Haist, H. J. Tiziani, *Opt. Commun.* **2000**, 185, 77.
- [121] V. Demergis, E.-L. Florin, *Nano Lett.* **2012**, 12, 5765.
- [122] J. Rodriguez, L. C. Davila Romero, D. L. Andrews, *Phys. Rev. A* **2008**, 78, 043805.
- [123] J. Ng, Z. Lin, C. T. Chan, P. Sheng, *Phys. Rev. B* **2005**, 72, 085130.
- [124] T. Cizmar, L. C. Davila Romero, K. Dholakia, D. L. Andrews, *J. Phys. B: Atom. Mol. Phys.* **2010**, 43, 102001.
- [125] T. M. Grzegorzczak, B. A. Kemp, J. A. Kong, *Phys. Rev. Lett.* **2006**, 96, 113903.
- [126] J. E. Melzer, E. McLeod, *Microsyst. Nanoeng.* **2021**, 7, 45.
- [127] E. McLeod, In *2023 Conf. on Lasers and Electro-Optics*, IEEE, San Jose, CA, USA, **2023**, pp. 1–2.
- [128] M. Waleed, *Master's Thesis*, The University of Queensland, Queensland Australia **2018**.
- [129] T. Badloe, I. Kim, Y. Kim, J. Kim, R. J., *Adv. Sci.* **2021**, 8, 2102646.
- [130] C. Pfeiffer, A. Grbic, *Phys. Rev. Lett.* **2013**, 110, 197401.
- [131] O. Tsilipakos, A. C. Tasolamprou, T. Koschny, M. Kafesaki, E. N. Economou, C. M. Soukoulis, *Adv. Opt. Mater.* **2018**, 6, 1800633.
- [132] O. Tsilipakos, T. Koschny, C. M. Soukoulis, *ACS Photonics* **2018**, 5, 1101.
- [133] N. Yu, P. Genevet, M. A. Kats, F. Aieta, J.-P. Tetienne, F. Capasso, Z. Gaburro, *Science* **2011**, 334, 333.
- [134] A. Alù, M. G. Silveirinha, A. Salandrino, N. Engheta, *Phys. Rev. B* **2007**, 75, 155410.
- [135] R. Melentiev, A. Wagih, A. Lagerweij, G. Mitteramskogler, G. Lubineau, C. A. Grande, *Virtual Phys. Prototyping* **2024**, 19, 23339368.
- [136] V.-C. Su, C. H. Chu, G. Sun, D. P. Tsai, *Opt. Express* **2018**, 26, 13148.
- [137] S. Chen, J. Chen, X. Zhang, Z.-Y. Li, J. Li, *Light: Sci. Appl.* **2020**, 9, 75.
- [138] Z. Liu, H. Du, J. Li, L. Lu, Z.-Y. Li, N. X. Fang, *Sci. Adv.* **2018**, 4, aat4436.
- [139] G. V. Naik, B. Saha, J. Liu, S. M. Saber, E. A. Stach, I. J. M. K., T. D. Sands, V. M. Shalae, A. Boltassaeva, *Proc. Nat. Acad. Sci. U.S.A.* **2014**, 111, 7546.
- [140] C. Ma, M. A. Escobar, Z. Liu, *Phys. Rev. B* **2011**, 84, 195142.
- [141] J. B. Pendry, *Phys. Rev. Lett.* **2000**, 85, 3966.
- [142] N. Garcia, M. Nieto-Vesperinas, *Phys. Rev. Lett.* **2002**, 88, 207403.
- [143] B. H. Chen, P. C. Wu, V.-C. Su, Y.-C. Lai, C. H. Chu, C. Lee, J.-W. Chen, Y. H. Chen, Y.-C. Lan, C.-H. Kuan, D. P. Tsai, *Nano Lett.* **2017**, 17, 6345.
- [144] S. Wang, P. C. Wu, V.-C. Su, Y.-C. Lai, C. H. Chu, J.-W. Chen, S.-H. Lu, J. Chen, B. Xu, C.-H. Kuan, T. Li, S. Zhu, D. P. Tsai, *Nat. Commun.* **2017**, 8, 187.
- [145] M. Kim, J. Rho, *Nano Converg.* **2015**, 2, 22.
- [146] J. M. Williams, *Phys. Rev. Lett.* **2001**, 87, 249703.
- [147] A. Grbic, G. V. Eleftheriades, *Phys. Rev. Lett.* **2004**, 92, 117403.
- [148] A. A. Houck, J. B. Brock, I. L. Chuang, *Phys. Rev. Lett.* **2003**, 90, 137401.
- [149] Z. Jacob, L. V. Alekseyev, E. Narimanov, *Opt. Express* **2006**, 14, 8247.
- [150] V. A. Podolskiy, E. E. Narimanov, *Phys. Rev. B* **2005**, 71, 201101.
- [151] V. A. Podolskiy, L. V. Alekseyev, E. E. Narimanov, *J. Mod. Optics* **2005**, 52, 2343.
- [152] A. A. Goyadinov, V. A. Podolskiy, *Phys. Rev. B* **2006**, 73, 155108.
- [153] D. Lu, Z. Liu, *Nat. Commun.* **2012**, 3, 1205.
- [154] C. Ma, Z. Liu, *Appl. Phys. Lett.* **2010**, 96, 183103.
- [155] C. Ma, Z. Liu, *Opt. Express* **2010**, 18, 4838.
- [156] N. Kundtz, D. R. Smith, *Nat. Mater.* **2010**, 9, 129.
- [157] P. Kumar, T. Ali, M. M. M. Pai, *IEEE Access* **2021**, 9, 18722.
- [158] M. Faenzi, G. Minatti, D. González-Ovejero, F. Caminita, E. Martini, C. D. Giovampaola, S. Maci, *Sci. Rep.* **2019**, 9, 10178.
- [159] H. Li, Z. Zhou, Y. He, W. Sun, Y. Li, I. Liberal, N. Engheta, *Nat. Commun.* **2022**, 13, 3568.
- [160] Y. Liu, T. Dong, X. Qin, W. Luo, N. Leng, Y. He, Y. Yuan, M. Bai, J. Z. J. Sun, Y. Li, *eLight* **2024**, 4, 4.
- [161] T. Jiang, H. Ning, H. Zhou, W. Hao, *2020 14th European Conf. on Antennas and Propagation (EuCAP)*, IEEE, Copenhagen, Denmark, **2020**, pp. 1–4.
- [162] R. S. Aziz, S. Koziel, A. Pietrenko-Dabrowska, *Sci. Rep.* **2024**, 14, 16037.
- [163] A. A. Musaed, S. S. Al-Bawri, W. M. Abdulkawi, Z. Y. K. Aljaloud, M. T. Islam, *Sci. Rep.* **2024**, 14, 290.
- [164] A. DiFalco, M. Ploschner, T. F. Kraus, *New J. Phys.* **2010**, 12, 113006.
- [165] C. Caloz, in *Metamaterial antennas and radiative systems*, (Eds: Y. M. A. Debatosh Guha), 1st ed., Wiley & Sons Ltd, New York **2010**, pp. 345–386.
- [166] R. Porath, *IEEE Trans. Ant. Prop.* **2000**, 48, 41.
- [167] C. Miliadis, R. B. Andersen, P. I. Lazaridis, Z. D. Zaharis, B. Muhammad, J. T. B. Kristensen, A. Mihovska, D. D. S. Hermansen, *IEEE Access* **2021**, 9, 89846.
- [168] J. S. Kula, D. Psychoudakis, W.-J. Liao, C.-C. Chen, J. L. Volakis, J. W. Halloran, *IEEE Antennas and Prop. Mag.* **2006**, 48, 13.
- [169] S. F. Mahmoud, *IEEE Ant. Wireless Prop. Lett.* **2004**, 3, 19.
- [170] M. E. Ermutlu, S. Tretyakov, *2005 IEEE Anten. Propagat. Soc. Int. Sympos.* **2005**, 2, 6.
- [171] J. S. Petko, D. H. Werner, In *IEEE Antennas and Propagation Society Int. Sympos.*, IET, Birmingham, UK **2005**, 77–81.
- [172] A. Alu, F. Bilotti, N. Engheta, L. Vegni, *IEEE Trans. Antennas Prop.* **2007**, 55, 13.
- [173] G. V. Eleftheriades, A. K. Iyer, P. C. Kremer, *IEEE Trans. Microwave Theor. Tech.* **2002**, 50, 2702.
- [174] A. Lai, T. Itoh, C. Caloz, *IEEE Microwave Mag.* **2004**, 5, 34.
- [175] C. A. Balanis, *Antenna Theory: Analysis and Design*, John Wiley & Sons, New York **2016**.

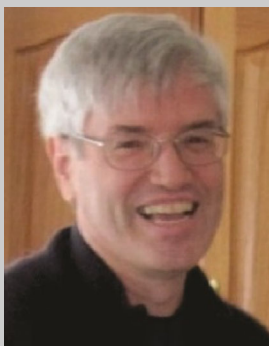
- [176] S. Enoch, G. Tayeb, P. Sabouroux, N. Gu erin, P. Vincent, *Phys. Rev. Lett.* **2002**, *89*, 213902.
- [177] P. K. Panda, D. Ghosh, *AEU – Int. J. Electron. Commun.* **2018**, *86*, 164.
- [178] E. Yablonovitch, T. J. Gmitter, K. M. Leung, *Phys. Rev. Lett.* **1991**, *67*, 2295.
- [179] Y. Xie, S. Ye, C. Reyes, P. Sithikong, B. I. Popa, B. J. Wiley, S. A. Cummer, *Appl. Phys. Lett.* **2017**, *110*, 181903.
- [180] D. Bourell, J. P. Kruth, M. Leu, G. Levy, D. Rosen, A. M. Beese, A. Clare, *CIRP Ann.* **2017**, *66*, 659.
- [181] C. M. Naraine, J. N. Westwood-Bachman, C. Horvath, M. Aktary, A. P. Knights, J. H. Schmid, P. Cheben, J. D. B. Bradley, *Laser Photonics Rev.* **2023**, *17*, 2200216.
- [182] Y. S. Tan, H. Wang, H. Wang, C. Pan, J. K. W. Yang, *Photon. Res.* **2023**, *11*, B103.
- [183] O. Yavas, M. Svedendahl, P. Dobosz, V. Sanz, R. Quidant, *Nano Lett.* **2017**, *17*, 4421.
- [184] X. Xiao, J. J. Yang, T. S. Millard, S. Zhu, K. M. Kowalczyk, J. W. G. Tisch, M. Matthews, S. A. Maier, R. F. Oulton, *ACS Photonics* **2024**, *11*, 2836.
- [185] M. Manocchio, M. Esposito, A. Passaseo, M. Cuscun a, V. Tasco, *Micromachines* **2021**, *12*, 6.
- [186] A. O. Krushynska, S. Janbaz, J. H. Oh, M. Wegener, N. X. Fang, *Appl. Phys. Lett.* **2023**, *123*, 240401.
- [187] M. Jeong, B. Ko, C. Jung, J. Kim, J. Jang, J. Mun, J. Lee, S. Yun, S. Kim, J. Rho, *Nano Lett.* **2024**, *24*, 5783.
- [188] L. J. Guo, *Adv. Mater.* **2007**, *19*, 495.
- [189] J. Kim, J. Seong, W. Kim, G.-Y. Lee, S. Kim, H. Kim, S.-W. Moon, D. K. Oh, Y. Yang, J. Park, J. Jang, Y. Kim, M. Jeong, C. Park, H. Choi, G. Jeon, K. Lee, D. H. Yoon, N. Park, B. Lee, H. Lee, J. Rho, *Nat. Mater.* **2023**, *22*, 474.
- [190] X. Cao, Y. Xiao, Q. Dong, S. Zhang, J. Wang, L. Wang, L. Gao, *Adv. Photon. Res.* **2022**, *3*, 2200127.
- [191] X. Zhang, S. Debnath, D.  . G uney, *J. Opt. Soc. Am. B* **2015**, *32*, 1013.
- [192] M. S. Rill, C. Plet, M. Thiel, I. Staude, G. von Freymann, S. Linden, M. Wegener, *Nat. Mater.* **2008**, *7*, 543.
- [193] X. X. Zeng, R. Wang, X. Q. Xi, B. Li, J. Zhou, *Opt. Express* **2018**, *26*, 17056.
- [194] J. Cen, Z. Deng, S. Liu, *Polym. Chem.* **2024**, *15*, 4599.
- [195] S. Matsuura, T. Hashimoto, *Opt. Microlithograph. XV, SPIE* **2002**, *4691*, 1433.
- [196] X. Wang, P. Tao, Q. Wang, R. Zhao, T. Liu, Y. Hu, Z. Hu, Y. Wang, J. Wang, Y. Tang, H. Xu, X. He, *Mater. Today* **2023**, *67*, 299.
- [197] C. K. Ober, F. K afer, C. Yuan, *Polymer* **2023**, *280*, 126020.
- [198] D. N. Le, T. Park, S. M. Hwang, J.-H. Kim, Y. C. Jung, N. Tiwale, A. Subramanian, W.-I. Lee, R. Choi, M. M. Sung, C.-Y. Nam, J. Kim, *Jpn. J. Appl. Phys.* **2023**, *62*, SG0812.
- [199] Y. Zhang, H. Yu, L. Wang, X. Wu, J. He, W. Huang, C. Ouyang, D. Chen, B. E. Keshta, *Adv. Colloid Interface Sci.* **2024**, *329*, 103197.
- [200] N. Fu, Y. Liu, X. Ma, Z. Chen, *J. Microelec. Manufact.* **2019**, *2*, 19020202.
- [201] H. Enkisch, J. Trenkler, *Europhys. News* **2004**, *35*, 149.
- [202] <https://fuse.wikichip.org/news/7375/tsmc-n3-and-challenges-ahead/> (accessed: May 2025).
- [203] A. Pirati, R. Peeters, D. Smith, S. Lok, M. van Noordenburg, R. van Es, E. Verhoeven, H. Meijer, A. Minnaert, J.-W. van der Horst, H. Meiling, J. Mallmann, C. Wagner, J. Stoeldraijer, G. Fisser, J. Finders, C. Zoldesi, U. Stamm, H. Boom, D. Brandt, D. Brown, I. Fomenkov, M. Purvis, *Extreme Ultraviolet (EUV) Lithography VII, SPIE* **2016**, *9776*, 78.
- [204] H. J. Levinson, *SPIE* **2019**, *11177*, 1117702.
- [205] H. J. Levinson, T. A. Brunner, *Int. Conf. Extreme UV Lithograph.* **2018**, *10809*, 5.
- [206] S.-S. Kim, R. Chalykh, H. Kim, S. Lee, C. Park, M. Hwang, J.-O. Park, J. Park, H. Kim, J. Jeon, I. Kim, D. Lee, J. Na, J. Kim, S. Lee, H. Kim, S.-W. Nam, *SPIE* **2017**, *10143*, 1014306.
- [207] K. Suzuki, K. Kitano, K. Ishizaki, S. Noda, *Opt. Express* **2014**, *22*, 17099.
- [208] M. J. Burek, N. P. de Leon, B. J. Shields, B. J. M. Hausmann, Y. Chu, Q. Quan, A. S. Zibrov, H. Park, M. D. Lukin, M. Lon car, *Nano Lett.* **2012**, *12*, 6084.
- [209] M. J. Burek, Y. Chu, M. S. Z. Liddy, P. Patel, J. Rochman, S. Meesala, W. Hong, Q. Quan, M. D. Lukin, M. Lon car, *Nat. Commun.* **2014**, *5*, 5718.
- [210] M. A. van de Haar, A. Polman, *Opt. Mater. Express, OME* **2016**, *6*, 884.
- [211] C. Weigel, U. Brokmann, M. Hofmann, A. Behrens, E. R adlein, M. Hoffmann, S. Strehle, S. Sinzinger, *JOM* **2021**, *1*, 040901.
- [212] M. Huff, *Micromachines* **2021**, *12*, 991.
- [213] T. Lill, *Atomic Layer Processing*, John Wiley & Sons, Ltd, New York, **2021**, pp. 133–224.
- [214] S. J. Fonash, *AIP Conf. Proc.* **1984**, *122*, 106.
- [215] H. Zhao, S. J. Park, B. R. Solomon, S. Kim, D. Soto, A. T. Paxson, K. K. Varanasi, A. J. Hart, *Adv. Mater.* **2019**, *31*, 1807686.
- [216] M. M. Hawkeye, M. T. Taschuk, M. J. Brett, *Glancing Angle Deposition of Thin Films: Engineering the Nanoscale*, John Wiley & Sons, New York **2014**.
- [217] C. Qu, J. L. Rozsa, H.-J. Jung, A. R. Williams, E. K. Markin, M. P. Running, S. McNamara, K. M. Walsh, *Sci. Rep.* **2023**, *13*, 207.
- [218] S. Bairagi, K. J arrendahl, F. Eriksson, L. Hultman, J. Birch, C.-L. Hsiao, *Coatings* **2020**, *10*, 768.
- [219] R. L. Puurunen, *Chem. Vap. Deposition* **2014**, *20*, 332.
- [220] E. C. Nwanna, S. Bitire, P. E. Imoisili, T.-C. Jen, *Int. J. Energy Res.* **2022**, *46*, 10499.
- [221] M. Liu, X. Li, S. K. Karuturi, A. I. Y. Tok, H. J. Fan, *Nanoscale* **2012**, *4*, 1522
- [222] M. Karbalaee Akbari, N. Siraj Lopa, S. Zhuiykov, *Coatings* **2023**, *13*, 1041.
- [223] H. Kim, H.-B.-R. Lee, W.-J. Maeng, *Thin Solid Films* **2009**, *517*, 2563.
- [224] M. Leskel a, M. Ritala, *Thin Solid Films* **2002**, *409*, 138.
- [225] P. Kelly, M. Liu, L. Kuznetsova, *Appl. Opt.* **2016**, *55*, 2993.
- [226] S. Clemmen, A. Hermans, E. Solano, J. Dendooven, K. Koskinen, M. Kauranen, E. Brainis, C. Detavernier, R. Baets, *Opt. Lett.* **2015**, *40*, 5371.
- [227] P. Paul, P. Schmitt, V. V. Sigurj onsd ottir, K. Hanemann, N. Felde, S. Schr oder, F. Otto, M. Gruenewald, T. Fritz, V. Roddatis, A. T unnermann, A. Szeghalmi, *ACS Appl. Mater. Interfaces* **2023**, *15*, 22626.
- [228] B. C. Mallick, C.-T. Hsieh, K.-M. Yin, Y. A. Gandomi, K.-T. Huang, *ECSS J. Solid State Sci. Technol.* **2019**, *8*, N55.
- [229] J. Dendooven, C. Detavernier, in *Atomic Layer Deposition in Energy Conversion Applications*, John Wiley & Sons, Ltd, New York **2017**, pp. 1–40.
- [230] M. Z. Ansari, P. Janicek, D. K. Nandi, S. Slang, M. Bouska, H. Oh, B. Shong, S.-H. Kim, *Appl. Surf. Sci.* **2021**, *565*, 150152.
- [231] P. O. Oviroh, R. Akbarzadeh, D. Pan, R. A. M. Coetzee, T.-C. Jen, *Sci. Technol. Adv. Mater.* **2019**, *20*, 465.
- [232] M. Z. Ansari, I. Hussain, D. Mohapatra, S. A. Ansari, R. Rahighi, D. K. Nandi, W. Song, S.-H. Kim, *Adv. Sci.* **2024**, *11*, 2303055.
- [233] T. Jeon, D.-H. Kim, S.-G. Park, *Adv. Mat. Interfaces* **2018**, *5*, 1800330.
- [234] I. Wathuthanthri, Y. Liu, K. Du, W. Xu, C.-H. Choi, *Adv. Func. Mater.* **2013**, *23*, 608.
- [235] D. Xia, Z. Ku, S. C. Lee, S. R. J. Brueck, *Adv. Mater.* **2011**, *23*, 147.
- [236] N. Feth, C. Enkrich, M. Wegener, S. Linden, *Opt. Express* **2007**, *15*, 501.
- [237] H. H. Solak, D. He, W. Li, S. Singh-Gasson, F. Cerrina, B. H. Sohn, X. M. Yang, P. Nealey, *Appl. Phys. Lett.* **1999**, *75*, 2328.

- [238] B. Buchroithner, D. Hartmann, S. Mayr, Y. J. Oh, D. Sivun, A. Karner, B. Buchegger, T. Griesser, P. Hinterdorfer, T. A. Klar, J. Jacak, *Nanoscale Adv.* **2020**, *2*, 2422.
- [239] Z. Vangelatos, M. E. Yildizdag, I. Giorgio, F. dell'Isola, C. Grigoropoulos, *Extreme Mech. Lett.* **2021**, *43*, 101202.
- [240] S.-W. Lee, M. Jafary-Zadeh, D. Z. Chen, Y.-W. Zhang, J. R. Greer, *Nano Lett.* **2015**, *15*, 5673.
- [241] J. Serbin, A. Ovsianikov, B. Chichkov, *Opt. Express* **2004**, *12*, 5221.
- [242] M. Grzelczak, J. Vermant, E. M. Furst, L. M. Liz-Marzán, *ACS Nano* **2010**, *4*, 3591.
- [243] M. Mayer, M. J. Schnepf, T. A. F. König, A. Fery, *Adv. Opt. Mater.* **2019**, *7*, 1800564.
- [244] S. Gomez-Graña, A. L. Beulze, M. Treguer-Delapierre, S. Mornet, E. Duguet, E. Grana, E. Cloutet, G. Hadziioannou, J. Leng, J.-B. Salmon, V. G. Kravets, A. N. Grigorenko, N. A. Peyyety, V. Ponsinet, P. Richetti, A. Baron, D. Torrent, P. Barois, *Mater. Horiz.* **2016**, *3*, 596.
- [245] M. A. Olson, A. Coskun, R. Klajn, L. Fang, S. K. Dey, K. P. Browne, B. A. Grzybowski, J. F. Stoddart, *Nano Lett.* **2009**, *9*, 3185.
- [246] M. A. Correa-Duarte, L. M. Liz-Marzán, *J. Mater. Chem.* **2006**, *16*, 22.
- [247] S. Vignolini, N. A. Yufa, P. S. Cunha, S. Guldin, I. Rushkin, M. Stefik, K. Hur, U. Wiesner, J. J. Baumberg, U. Steiner, *Adv. Mater.* **2012**, *24*, OP23.
- [248] S. Fang, N. Xu, L. Zhou, T. Wei, Y. Yang, Y. Liu, J. Zhu, *Sci. Adv.* **2024**, *10*, adl1896.
- [249] K. Lodewijks, N. Verellen, W. Van Roy, V. Moshchalkov, G. Borghs, P. Van Dorpe, *Appl. Phys. Lett.* **2011**, *98*, 091101.
- [250] J.-H. Huh, J. Lee, S. Lee, *Nano Lett.* **2020**, *20*, 4768.
- [251] K. A. Forbes, D. S. Bradshwa, D. L. Andres, *J. Nanophotonics* **2019**, *9*, 1.
- [252] P. Pandey, M. Dahiya, *J. Crit. Rev.* **2016**, *3*, 18.
- [253] J. P. Rao, K. E. Geckeler, *Prog. Polym. Sci.* **2011**, *36*, 887.
- [254] V. Harish, M. M. Ansari, D. Tewari, M. Gaur, A. B. Yadav, M.-L. García-Betancourt, F. M. Abdel-Haleem, M. Bechelany, A. Barhoum, *Nanomaterials* **2022**, *12*, 3226.
- [255] H. Ghorbani, F. Mehr, H. Pazoki, B. Rahmani, *Orient. J. Chem.* **2015**, *31*, 1219.
- [256] M. Hijaz, S. Das, I. Mert, A. Gupta, Z. Al-Wahab, C. Tebbe, S. Dar, J. Chhina, S. Giri, A. Munkarah, S. Seal, R. Rattan, *BMC Cancer* **2016**, *16*, 220.
- [257] V. Srivastava, D. Gusain, Y. C. Sharma, *Ceram. Int.* **2013**, *39*, 9803.
- [258] M. Kundu, G. Karunakaran, N. Van Minh, D. Kuznetsov, *J. Clust. Sci.* **2017**, *28*, 1285.
- [259] H. Hayashi, Y. Hakuta, *Materials* **2010**, *3*, 3794.
- [260] P. B. Dahivade, S. N. Pawar, H. M. Pathan, B. J. Lokhande, *ES Energy Environ.* **2024**, *24*, 1098.
- [261] S. F. Rafie, H. Sayahi, H. Abdollahi, N. Abu-Zahra, *Mater. Today Commun.* **2023**, *37*, 107589.
- [262] N. Abid, A. M. Khan, S. Shujait, K. Chaudhary, M. Ikram, M. Imran, J. Haider, M. Khan, Q. Khan, M. Maqbool, *Adv. Colloid Interface Sci.* **2022**, *300*, 102597.
- [263] G. Yang, S.-J. Park, *Materials* **2019**, *12*, 1177.
- [264] D. G. Duff, A. Baiker, P. P. Edwards, *Langmuir* **1993**, *9*, 2301.
- [265] P. D. Nallathamby, J. Hopf, L. E. Irimata, T. L. McGinnity, R. K. Roeder, *J. Mat. Chem. B.* **2016**, *4*, 5418.
- [266] M. A. Malik, M. Y. Wani, M. A. Hashim, *Arab. J. Chem.* **2012**, *5*, 397.
- [267] J. Eastoe, M. J. Hollamby, L. Hudson, *Adv. Colloid Interface Sci.* **2006**, *5*, 128.
- [268] J. A. López Pérez, M. A. López Quintela, J. Mira, J. Rivas, S. W. Charles, *J. Phys. Chem. B* **1997**, *101*, 8045.
- [269] S. Dekkar, *Chem. Africa* **2024**, *7*, 1.
- [270] M. Malekzadeh, M. T. Swihart, *Chem. Soc. Rev.* **2021**, *50*, 7132.
- [271] S.-J. Shih, I.-C. Chien, *Powder Technol.* **2013**, *237*, 436.
- [272] M. U. Zahid, E. Pervaiz, A. Hussain, M. I. Shahzad, M. B. K. Niazi, *Mater. Res. Express* **2018**, *5*, 052002.
- [273] A. B. Workie, H. S. Ningsih, S.-J. Shih, *J. Anal. Appl. Pyrolysis* **2023**, *170*, 105915.
- [274] T.-H. Kim, H.-K. Song, S. Kim, *Nanotechnology* **2019**, *30*, 275603.
- [275] M. Gracia-Pinilla, E. Martínez, G. S. Vidaurri, E. Pérez-Tijerina, *Nanoscale Res. Lett.* **2009**, *5*, 180.
- [276] A. Hembem, I. Chianella, G. J. T. Leighton, *Bioeng.* **2021**, *8*, 38.
- [277] E. Pérez-Tijerina, M. G. Pinilla, S. Mejía-Rosales, U. Ortiz-Méndez, A. Torres, M. José-Yacamán, *Faraday Disc.* **2008**, *138*, 353.
- [278] R. López-Martín, B. S. Burgos, P. S. Normile, J. A. De Toro, C. Binns, *Nanomaterials (Basel)* **2021**, *11*, 2803
- [279] T. H. L. Nghiem, T. N. Le, T. H. Do, T. T. D. Vu, Q. H. Do, H. N. Tran, *J. Nanoparticle Res.* **2013**, *15*, 2091.
- [280] R. G. Chaudhuri, S. Paria, *Chem. Rev.* **2012**, *112*, 2373.
- [281] M. A. Baqir, P. K. Choudhury, Q. A. Naqvi, *Optik* **2021**, *246*, 167850.
- [282] H. Zhang, Y. Li, X. Long, J. Luo, Y. Zhang, M. Song, J. Fang, C. Guan, Y. Cheng, H. Liu, *J. Mater. Chem. C* **2020**, *8*, 12876.
- [283] H. Giesche, *J. Eur. Ceram. Soc.* **1994**, *14*, 205.
- [284] W. Stober, A. Fink, E. Bohn, *J. Colloid Interface Sci.* **1968**, *26*, 62.
- [285] Editorial, *Nat. Comput. Sci.* **2024**, *4*, 543.
- [286] A. Alex-Amor, Á. Palomares-Caballero, C. Molero, *Nat. Comput. Sci.* **2024**, *4*, 543.
- [287] R. Dharmavarapu, S. H. Ng, F. Eftekhari, S. Juodkazis, S. Bhattacharya, *Opt. Express* **2020**, *28*, 3505.
- [288] D. R. Smith, S. Schultz, P. Markos, C. M. Soukoulis, *Phys. Rev. B* **2002**, *65*, 195104.
- [289] B. Edwards, A. Alu, M. G. Silveirinha, N. Engheta, *J. Appl. Phys.* **2009**, *105*, 044905.
- [290] A. Stewart, Y. Zhu, Y. Liu, D. A. Simpson, P. J. Reece, *Nano Lett.* **2024**, *24*, 12188.
- [291] K. Visscher, S. P. Gross, S. M. Block, *IEEE J. Sel. Top. Quantum Electron.* **1996**, *2*, 1066.
- [292] M. T. Valentine, N. R. Gyuosh, B. Gutierrez-Medina, A. N. Fehr, J. O. Andreasson, S. M. Block, *Opt. Lett.* **2008**, *33*, 599.
- [293] C. Maurer, A. Jesacher, S. Bernet, M. Ritsch-Marte, *Laser Photonics Rev.* **2011**, *5*, 81.
- [294] X. Li, Y. Yang, S. Yan, W. Gao, Y. Zhou, X. Yu, C. Bai, D. Dan, X. Xu, B. Yao, *Photonix* **2024**, *5*, 32.
- [295] X. Yun, Y. Liang, M. He, L. Guo, X. Zhang, T. Zhao, P. R. Bianco, M. Lei, *Opt. Express* **2023**, *31*, 19613.
- [296] K. Sasaki, M. Koshioka, H. Misawa, N. Kitamura, H. Masuhara, *Opt. Lett.* **1991**, *16*, 1463.
- [297] Y. Wang, S. Shevate, T. M. Wintermantel, M. Morgado, G. Lochead, S. Whitlock, *npj Quantum Inf.* **2020**, *6*, 1.
- [298] V. Garcés-Chávez, D. McGloin, H. Melville, W. Sibbett, K. Dholakia, *Nature* **2002**, *419*, 145.
- [299] G. Akselrod, W. Timp, U. Mirsaidov, Q. Zhao, C. Li, R. Timp, K. Timp, P. Matsudaira, G. Timp, *Biophys. J.* **2006**, *91*, 3465.
- [300] U. Mirsaidov, J. Scrimgeour, W. Timp, K. Beck, M. Mir, P. Matsudaira, G. Timp, *Lab Chip* **2008**, *8*, 2174.
- [301] M. Lee, H. Hugonnet, M. J. Lee, Y. Cho, Y. Park, *Biophys. Rev.* **2023**, *4*, 011302.
- [302] K. J. Mitchell, S. Turtaev, M. J. Padgett, T. Cižmar, D. B. Phillips, *Opt. Express* **2016**, *24*, 29269.
- [303] C. Maurer, A. Jesacher, S. Bernet, M. Ritsch-Marte, *Laser Photon. Rev.* **2011**, *5*, 81.
- [304] M. S. Woody, M. Capitanio, E. M. Ostap, Y. E. Goldman, *Opt. Express.* **2018**, *26*, 11181.
- [305] G. Sinclair, P. Jordan, J. Courtial, M. Padgett, J. Cooper, Z. J. Laczik, *Opt. Express* **2004**, *12*, 5475.
- [306] L. A. Shaw, R. M. Panas, C. M. Spadaccini, J. B. Hopkins, *Opt. Lett.* **2017**, *42*, 2862.

- [307] S. Chizari, M. P. Lim, L. A. Shaw, S. P. Austin, J. B. Hopkins, *Small* **2020**, *16*, 2000314.
- [308] D. C. Benito, D. M. Carberry, S. H. Simpson, G. M. Gibson, M. J. Padgett, J. G. Rarity, M. J. Miles, S. Hanna, *Opt. Express* **2008**, *16*, 13005.
- [309] K. Visscher, G. J. Brakenhoff, J. J. Krol, *Cytometry* **1993**, *14*, 105.
- [310] K. Sarveswarn, V. Kurz, Z. Dong, T. Tanaka, S. Penny, G. Timp, *Sci. Rep.* **2016**, *6*, 21885.
- [311] Y-H. Wu, H. B. Park, T. Kai, B. D. Freeman, D. S. Kalika, *J. Membrane Sci.* **2010**, *347*, 197.
- [312] J. J. Bohn, M. Ben-Moshe, A. Tikhonov, D. Qu, D. N. Lamont, S. A. Asher, *J. Colloid Interface Sci.* **2010**, *344*, 298.
- [313] M. S. Wheeler, J. S. Aitchison, M. Mojahedi, *Phys. Rev. B* **2005**, *72*, 193103.
- [314] M. F. Limonov, M. V. Rybin, A. N. Poddubny, Y. S. Kivshar, *Nat. Photonics* **2017**, *11*, 543.



**Apurba Paul** is a Postdoctoral Research Associate in the Department of Electrical Engineering at the University of Notre Dame, where he works under the guidance of Prof. Gregory Timp. His research lies at the intersection of biophysics and nanotechnology, with a particular focus on optical trapping and nanopore-based single-molecule spectroscopy. He received his Ph.D. in Physics from the Indian Institute of Science, Bangalore, under the mentorship of Prof. Vasant Natarajan. Before joining Notre Dame, he held a postdoctoral position in the Department of Physics and Astronomy at Clemson University.



**Gregory Timp** received his Ph.D. from the Massachusetts Institute of Technology working with Mildred Dresselhaus to measure the physical properties of graphite intercalation compounds. After a postdoc at IBM working with Alan Fowler, he joined Bell Laboratories, where he pursued transport physics in nanostructures along with optical trapping of atoms. In 2010, he joined the Notre Dame faculty. His research there focuses mainly on the application of semiconductor nanotechnology to address questions in biology. He is a Fellow of AAAS; APS; and IEEE. He has published over 100 articles in scientific journals and holds 10 patents.